Journal of MATERIALS RESEARCH

Invited Feature Paper - Review
DOI: 10.1557/jmr.2019.347

ATOMIC LAYER DEPOSITION FOR EMERGING THIN-FILM MATERIALS AND APPLICATIONS

FOCUS ISSUE

Atomic layer deposition for nonconventional nanomaterials and their applications

Taewook Nam[1] Hyungjun Kim[1,a)]

[1]School of Electrical and Electronic Engineering, Yonsei University, Seoul 03722, Republic of Korea
[a)]Address all correspondence to this author. e-mail: hyungjun@yonsei.ac.kr
This paper has been selected as an Invited Feature Paper.
Received: 1 September 2019; accepted: 7 October 2019

Amorphous carbon, germanium oxide, and 2-dimensional transition metal dichalcogenides grown by atomic layer deposition (ALD) are considered as promising materials for advanced nanoscale device fabrication processes and electronic devices, owing to their extraordinary characteristics. Deposition of these materials using ALD can overcome the limitations of current deposition techniques, including poor step coverage and wafer-scale uniformity, and uncontrollable stoichiometry. Despite these advantages, there has been a lack of research into these materials due to the absence of suitable precursors or optimized processes. In this review, we focus on these nonconventional materials, which have rarely been studied using ALD. The latest research progress and future outlook on these materials grown by ALD will be highlighted, with a particular focus on the applications of future nanoscale device fabrication processes and new concepts in device fabrication which could lead to a paradigm shift in electronics.

Introduction

Ever since the introduction of atomic layer epitaxy by Suntola [1], numerous research on atomic layer deposition (ALD) have been conducted for a wide range of applications, including semiconductor applications in display, catalysis, functional coating, and medical and pharmaceutical applications [2, 3, 4, 5, 6, 7, 8, 9, 10, 11, 12]. ALD is a self-limiting thin film deposition method based on surface-saturated reactions between chemical species, and it possesses a number of advantages when compared with other deposition methods (e.g., sputtering and CVD). These advantages are, for instance, the controllability of atomic-level thickness, excellent conformality, and large-area uniformity [6]. Although, owing to these advantages, ALD has become an indispensable technique for the fabrication of nanoscale devices, it was not in the spotlight when it was introduced due to low productivity. When scaling down of devices and thin film deposition of sub-nanometer thickness on a high-aspect-ratio substrate or 3D complex structure with excellent conformality were required, ALD became the main deposition technique for the fabrication of nanoscale devices. At the same time, many research groups tried to overcome the issue of low productivity by changing from a conventional temporal to a spatial ALD process [13]. Owing to these numerous efforts, ALD has become one of the important deposition techniques in many industries.

From the recently published bibliometric analysis on ALD process, it can be seen that the number of publications on ALD has significantly increased from the early 2000s [14]. Metal oxides and nitride materials are the most studied materials among the reported ALD-grown materials. Deposition of metal oxides and nitrides using ALD is, therefore, the most prevalent, and this might be due to the importance of these materials for the fabrication of Si-based electronics, including gate dielectric [15, 16, 17] or diffusion barrier for interconnects [18, 19, 20]. Some conductive oxides (e.g., ZnO and In_2O_3) have also been considered as transparent conductive oxides or channel materials in displays [21, 22, 23, 24]. Tens of metal oxides, on the other hand, have been developed for functional coatings [25, 26, 27] and energy or environmental applications [3, 5, 10]. In addition, various metals have been studied for the purpose of diffusion barrier, seed/adhesion layer, catalyst, and ultrathin conductive coating [11, 26, 28, 29]. Even though a number of materials have been developed for diverse applications, most research still focus on a limited number of materials, which may be due to the lack of need for new materials or precursors for deposition. As new concepts have been developed for

https://doi.org/10.1557/jmr.2019.347 Published online by Cambridge University Press

© Materials Research Society 2019

improving processing and devices, such as hard mask for multiple patterning [30, 31, 32], secure memory storage fabrication [33, 34], or neuromorphic devices which can overcome the current limitation of Si-based devices [35, 36, 37], it is highly desirable to develop a nonconventional material deposition process based on ALD.

In this review, growth of nonconventional materials that have been rarely studied with ALD will be highlighted. We will discuss the recent progress of growing amorphous carbon (a-C), germanium oxide (GeO_2), and 2D transition metal dichalcogenides (2D TMDCs) by the ALD process. These materials have been highlighted recently as new concepts for processing and emerging devices. We will briefly describe the need for these materials at the beginning of each section, followed by recent progress and outlook.

Recent progress on nonconventional material deposition using ALD

Amorphous carbon

Carbon is one of the most common elements on earth, and it exists in various forms by bonding with each other in different ways, known as allotropes of carbons [14]. There are many different types of carbon allotropes, and they show considerably different characteristics. These characteristics are comparable to those of the allotropes of other elements [38, 39, 40]. Diamond, for instance, one of the well-known allotropes of carbon with sp^3 configuration, is mainly used in industry for grinding or polishing, owing to its superior hardness from its bonding configuration [41, 42]. Graphite is a crystalline form of carbon arranged in a hexagonal structure with 3-fold coordinated sp^2 configuration. Most of the carbon species exist as graphite under standard condition, showing high stability. Due to its high conductivity and excellent stability, graphite is frequently used as electrodes for batteries or refractory material [40, 43]. Graphene, which has been recently discovered as another allotrope of carbon with 2D honeycomb structures, shows excellent electrical conductivity, even though the thickness of the material is less than a nanometer [41]. Carbon-based materials, therefore, show diverse characteristics depending on their structures, which can be applicable to various applications, especially when we can modulate the crystal structures of carbon.

a-C, a randomly hybridized carbon with sp^3 and sp^2 configurations, is one of the most fascinating materials for the hard mask for multiple patterning processes [44, 45, 46], owing to its etch selectivity, hardness, and cost-effectiveness. As devices are being scaled down, photolithography encounters the physical limitation for sub-40 nm device fabrication [47, 48]. This limitation can be overcome by changing the light source to extreme ultraviolet (EUV), which enables the resolution of patterning below 10 nm. However, because of technical immaturity and poor cost-effectiveness, multiple patterning has been adapted on sub-20 nm device patterning, instead of EUV lithography [30]. Double patterning, one of the multiple patterning processes that were initially adopted, forms a fine pattern by patterning the same pitch twice, making a pattern size in half. In this patterning process, a-C is an essential material since a-C hard mask can resist any dry etch chemistry during the multiple patterning process with its superior etch selectivity, and it can be simply removed by oxygen plasma ashing without leaving behind any residue [49, 50, 51, 52]. Currently, most of the a-C deposition is conducted by plasma-enhanced chemical vapor deposition (PE-CVD), which ensures high-throughput [45, 51]. As technology node decreases to the sub-10-nm scale, a further complex patterning process, i.e., quadruple, sextuple, or octuple patterning, is required [53, 54], and a deposition technique that ensures excellent conformality on the high-aspect-ratio structure spacer is needed for a-C deposition.

To obtain a single-element material using an ALD process, all ligands of the precursor core metal should be detached by the reaction with surface reactive species or subsequent reducing agents. In the early 2000s, Rossnagel and Kim reported a plasma-enhanced ALD (PE-ALD)–based Ta and Ti deposition using halide precursors and hydrogen radicals [55, 56]. In these studies, hydrogen radicals generated by H_2 plasma have been suggested as promising reactants for single element deposition because of the high reducing ability of the hydrogen radicals. Even though the hydrogen radicals have excellent reactivity, a proper precursor selection is still important for a single-element material deposition using ALD. In these reports, a reaction between halide ligands and hydrogen radicals was available because of the high reactivity of halide ligands, forming volatile H–X by-products, where X is a halide [57]. The bond dissociation energy is dependent on the ligand, and that means the external energy (e.g., heat) for the detachment of precursor ligands by hydrogen radicals could be increased, resulting in a high process temperature [58, 59, 60, 61]. Although the reaction energy is not directly related to the bond dissociation energy, a comparison with the energy required to dissociate a given species is still meaningful. In addition, some of the halide compounds that are formed during the reaction show stability at room temperature, hindering the adsorption of the subsequent precursors or reactants [62]. For these reasons, it is critical to choose an adequate precursor whose ligand can be detached at a relatively low temperature without leaving any by-products on the surface. Thus, the selection of the precursor with adequate ligands is important to obtain pure single-element material deposition by ALD.

https://doi.org/10.1557/jmr.2019.347 Published online by Cambridge University Press

© Materials Research Society 2019

There have been only a couple of reports on carbon deposition using the ALD method. Hukka et al. reported a radical-enhanced ALD of carbon on a diamond substrate using chlorocarbon radicals, which were generated from a $CHCl_3$ and H_2 mixture, as a precursor and atomic hydrogen as a reactant from 850 to 950 °C [63]. Komarov et al. also reported radical ALD-based carbon on a Mo substrate using CF_x radicals, which were generated via a reaction with dissociated hydrogen and CF_4, as a carbon source from 710 to 760 °C [64]. Both studies, however, did not show self-limiting growth and focused on the growth of crystalline carbon (denoted as diamond in these manuscripts), instead of an a-C film. The morphologies of the grown films are considerably rough, unlike that of the thin film grown by ALD. Because of the high bond dissociation energy of CF_x, a relatively high temperature is needed for carbon growth in order to detach the ligands from the precursor. Deleterious by-products from the reaction [e.g., hydrofluoric acid (HF) and HCl] are other obstacles for the adaptation to mass production.

Recently, Choi et al. reported ALD-based a-C deposition using a halide precursor and hydrogen radical on a relatively low temperature region [65]. Among various halide precursors, CBr_4 precursor was chosen as the halide precursor for a-C growth, since the bond dissociation energy between C and Br is suitable for the ALD process, which is approximately 234 kJ/mol, which is much lower than that of CF_4 or CCl_4 (approximately 519 and 297 kJ/mol, respectively). For this reason, CBr_4 had also been used as a carbon source for the 3–5 compound doping (e.g., GaAs) because of high reactivity [66, 67]. Moreover, bromocarbons that are formed after an ALD reaction (e.g., $CHBr_3$ and CH_2Br_2) can be easily decomposed by the reactions with hydrogen radicals, and these decomposed species can be favorably vacuumed out in the gas phase [61, 66, 68]. Although carbon tetraiodide (CI_4) has a lower bond dissociation energy (approximately 180 kJ/mol), it might not be compatible for an ALD process because of the strong acidity of its by-products (hydrogen iodide), which might have deleterious effects on the film growth [69, 70]. a-C deposition using CBr_4 on an untreated SiO_2 substrate showed poor nucleation of carbon, whereas a number of carbon nuclei were observed on the O_2 plasma–treated SiO_2 substrate, as shown in Fig. 1(a) and 1(b). The number of nuclei increased when the CBr_4 was exposed on the O_2 plasma–treated surface for 2 min, and completely uniform a-C was deposited when the exposure time of the CBr_4 was 4 min. The similar nucleation during ALD occurs frequently in ALD noble metal growth [71, 72, 73, 74, 75] because of the lack of adsorption sites [76, 77], or the large difference in the surface energy between the substrate and the metal element [78, 79]. There are several reports on the pretreatment of the substrate for facilitating nucleation during the ALD process, such as the UV/O_3 [80], chemical [81], or plasma treatment [82] prior to the ALD. Pretreatment of the surface by CBr_4 exposure also helps to form a uniform carbon film during the initial ALD growth stage.

The growth characteristics of a-C were systemically investigated as a function of precursor exposure time and substrate temperature on a 2-step surface pretreated SiO_2 substrate, as shown in Figs. 1(e) and 1(f). Unlike previous reports that a reliable ALD growth mode had not been achieved, ALD a-C using CBr_4 shows growth saturation when the precursor exposure time is over 14 s, and the saturated growth rate of ALD a-C is 0.14 Å/cycle at 300 °C. The growth of ALD a-C shows a stable growth rate from 250 to 300 °C, and when the growth temperature exceeds 350 °C, CBr_4 molecules start to dissociate into reactive CBr_x ($x < 4$) because of the weak C–Br bonds [33, 34], losing its self-limiting growth nature. Since ALD ensures superior step coverage of thin films on a high aspect ratio structure owing to its peculiar growth mechanism, self-limiting growth of ALD a-C can be deposited inside via holes with excellent conformality (>90%).

In a Raman analysis of an ALD-grown a-C film, as shown in Fig. 2(a), every spectrum showed similar shape, regardless of the growth temperature. By deconvolution of the Raman spectrum of a-C grown at 300 °C, the mixed phase of nanocrystalline diamond (1650 cm^{-1}), diamond (1340 cm^{-1}), and disordered sp^3 carbon (1500 cm^{-1}) was assigned to the deconvoluted Raman peaks, which corresponds to the well-known D, G, and D′ peaks, respectively. The presence of D, G, and D′ peaks in a single Raman spectrum of a-C indicates the ALD a-C film contains both nanocrystalline sp^3 and sp^2 graphitic carbon [83]. X-ray photoelectron spectroscopy (XPS) was used to characterize an ALD-grown a-C film at 200 and 300 °C, as shown in Fig. 2(b). In deconvoluted C 1*s* spectra, various C peaks, including sp^2 graphitic carbon (284.6 eV), C–C (285.3 eV), C–O, or C–Br (286.1 eV), are observed regardless of the growth temperature. In the case of Br 3*p* spectra, two peaks at 183.2 and 190.1 eV are clearly observed when the growth temperature of a-C was 200 °C, but not at 300 °C. This indicates that an ALD a-C film grown at 200 °C contains some bromine residue, whereas the amount of bromine at 300 °C is negligible. In a quantitative analysis of the XPS spectra, a-C growth at 200 °C contains a significant amount of oxygen and bromine impurities in the film (approximately 17 and 2 at.%, respectively), whereas the a-C growth at 300 °C shows incorporation of less oxygen (approximately 9 at.%) with negligible bromine impurities. Since the reaction between CBr_4 and atomic hydrogen is facilitated as the growth temperature increases, the remaining impurity (i.e., bromine) is much less when the growth temperature is 300 °C. Incorporation of a large amount of oxygen in the a-C growth at 200 °C might be originated from the ambient air, and the large portion of minor carbon species (e.g., C–C, C–O, or C=O)

https://doi.org/10.1557/jmr.2019.347 Published online by Cambridge University Press

© Materials Research Society 2019

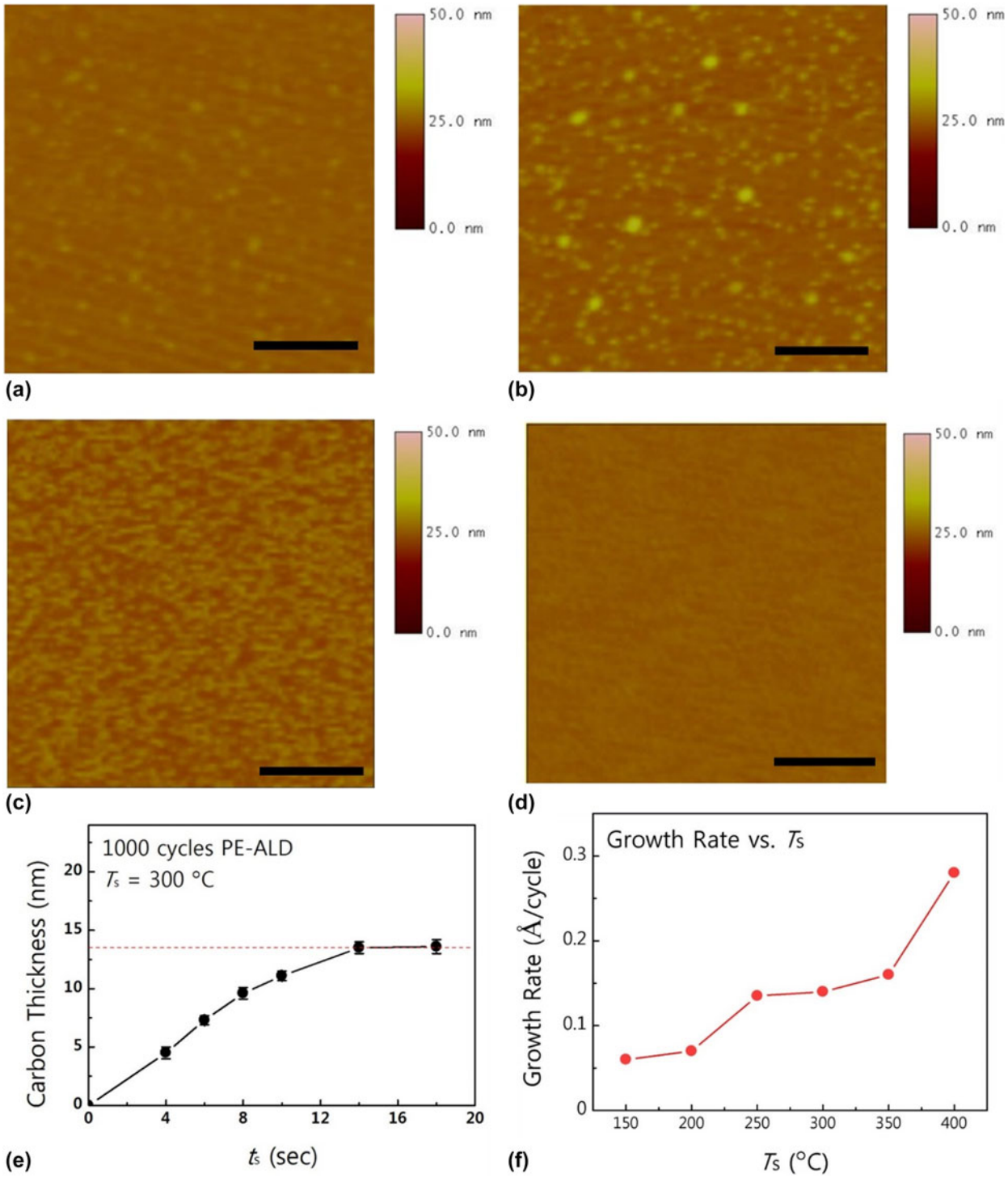


Figure 1: AFM images of a-C films grown by PE-ALD using CBr_4 on (a) bare SiO_2 substrate without pretreatment, (b) hydroxylated SiO_2 with in situ O_2 plasma pretreatment, and (c), (d) hydroxylated SiO_2 pre-exposure to CBr_4 for 2 and 4 min, respectively. (e) Thickness of ALD a-C as a function of precursor exposure time and (f) growth rates as a function of growth temperature. Reprinted from Ref. 65 with permission from Elsevier.

might have contributed to an increase in oxygen incorporation. In the Fourier-transform infrared (FT-IR) spectroscopy for measuring bonding characteristics of a-C [Fig. 2(c)], a couple of peaks indicating carbonaceous species are observed, which corresponds to sp^3 C–C stretching/C–H bending (1037 cm^{-1}), sp^3 C–H/C–O stretching (1105–1375 cm^{-1}), sp^2 C=C vibration (1614 cm^{-1}), and C–Br stretching vibration (500–800 cm^{-1}). In a microstructure analysis of an ALD a-C grown at 300 °C using transmission electron microscopy, as shown in Fig. 2(d), nano-graphitic fringes with intermixed sp^2 and sp^3 carbon

https://doi.org/10.1557/jmr.2019.347 Published online by Cambridge University Press

© Materials Research Society 2019

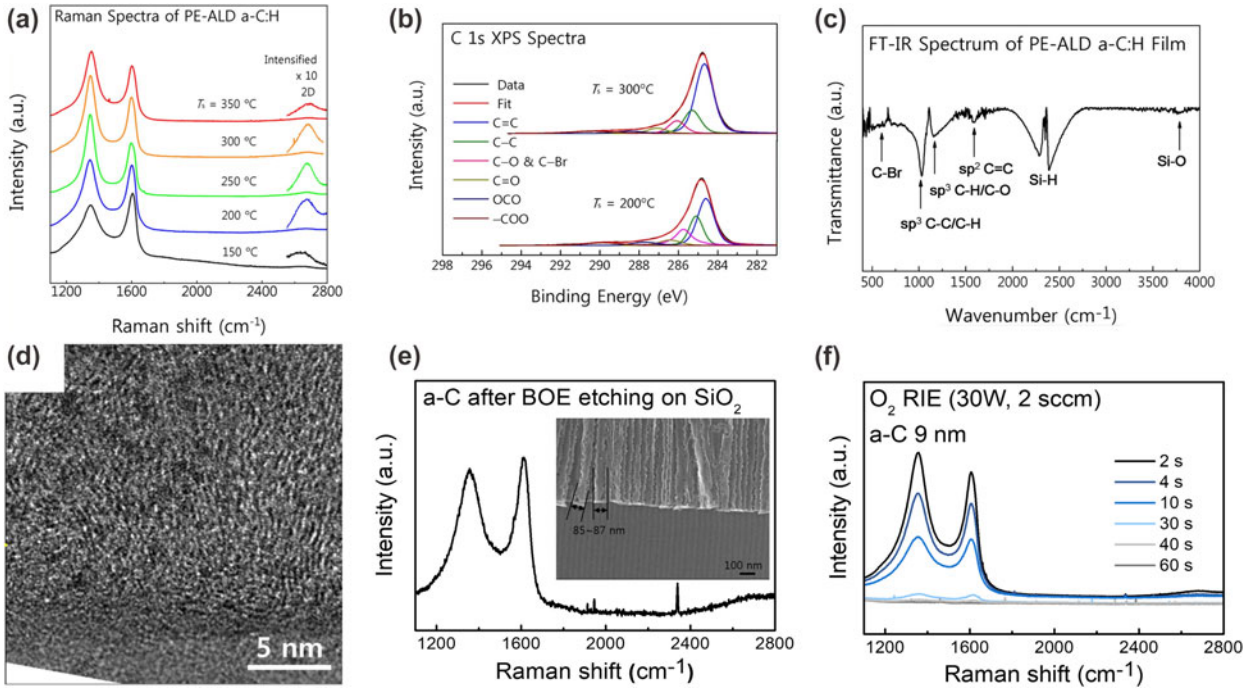


Figure 2: (a) Raman and (b) XPS C 1*s* spectra of ALD a-C as a function of deposition temperature, and (c) FT-IR spectrum of ALD a-C grown at 300 °C. (d) HR-TEM image of a-C deposited on SiO_2 substrate and Raman spectra of ALD a-C after (e) 1 min of diluted BOE etching (D.I. water:HF = 100:1) and (f) after O_2 plasma as a function of ashing time. Reprinted from Ref. 65 with permission from Elsevier.

lattices are observed, which matches the results from Raman spectroscopy. From these analyses of a-C, ALD a-C using CBr_4 and H_2 plasma can form high-quality a-C consisting of hydrogenated nanocrystalline sp^3 carbon and non-hydrogenated sp^2 carbon with incorporation of a small amount of oxygen and bromine.

The electrical properties of a-C were also characterized, and the possibility of using them for conformal conductive coating was investigated. The resistivity of ALD a-C grown at 200 and 300 °C, measured by the 4-point probe, was 1.62 and 0.25 Ω cm, respectively. In the same study, a bottom-gated transistor was fabricated, in which the channel is an a-C thin film grown at 200 and 300 °C, in order to further characterize the electrical properties. In the transfer curve, it can be seen that a-C shows weak p-type behavior regardless of the growth temperature. This p-type characteristic of a-C is generally observed in the other reports on diamond-like carbon or nanocrystalline graphitic carbon [40, 84]. The calculated field-effect mobility of the 300 °C grown a-C transistor was 1.7 cm^2/V s, whereas that of the transistor grown at 200 °C was 0.1 cm^2/V s. The high resistivity and poor field-effect mobility of the a-C grown at 200 °C originated from the incorporation of a large amount of oxygen and bromine impurities, which deteriorate the electrical properties of a-C.

As mentioned in the introduction of this section, a-C is one of the essential materials for a multiple-patterning process, owing to its superior etch selectivity and ashability. These superior characteristics of ALD-grown a-C are proven by experiments. Figure 2(e) shows the Raman spectrum and the scanning electron microscopy image of an 18-nm-thick ALD a-C after buffered oxide etchant (BOE) etching on 100–500 nm SiO_2 via hole substrate. After 1 min of BOE etching, the Raman spectrum remained unchanged, and the deposited a-C retained its structure when SiO_2 was entirely etched by BOE, indicating a-C is resistant to HF. In addition, the deposited a-C was perfectly removed after 60 s of O_2 reactive ion etching, as shown in Fig. 2(f). Both results demonstrated that ALD a-C using CBr_4 precursor can be applied to the hard mask deposition for advanced multiple patterning, which requires a deposition technique that ensures high conformality.

In this section, the growth and film properties of a-C by ALD are discussed. Even though there is a lack of research on ALD-based a-C deposition to this day, conformal coating of a-C using ALD is considered a promising hard mask deposition technique for an advanced multiple-patterning process, which requires a coating technique with excellent step coverage, owing to its superior etch selectivity and ashability. Moreover, ALD-grown a-C shows good electrical properties and excellent conformality at a relatively low temperature compared to chemical vapor deposition (CVD), which can be applicable for various fields, such as conductive coating for 3D complex battery electrodes and corrosion resistive coating on electrochemical devices [85, 86, 87]. In particular, ALD-based a-C deposition on a lithium ion battery electrode is expected to be

https://doi.org/10.1557/jmr.2019.347 Published online by Cambridge University Press

© Materials Research Society 2019

an effective coating that can help increase electrode conductivity, facilitate surface chemistry of active materials, and protect the electrode from direct contact with the electrolyte, leading to enhanced cycle life and ratio capability of batteries. Precise thickness control of carbon coating is essential in this case since a thick carbon coating layer would act as a barrier for Li^+ diffusion, while a thin layer would hardly form a full coating layer on the surface of the substrate, leading to an increase in sheet resistance [85]. The application of ALD a-C coating can be extended to other materials having complex structures, which in turn enables an improvement of not only the process but also the performance of the devices.

Germanium oxide

In solid-state devices, Ge has been considered as a promising candidate for replacing Si, which can then overcome the current limitation of Si-based electronics. This is due to the high electron and hole mobility of Ge, making Ge-based electronics devices that operate at the high speed possible [88, 89, 90]. Despite these advantages of Ge, Ge-based electronics cannot be fabricated. One of the biggest problems of use of this material for device fabrication is its undesirable interfacial layer [88]. When a high-*k* dielectric material is deposited on the Ge substrate by using ALD, the interfacial layer that is formed between the Ge and dielectric, caused by Ge diffusion, generates high defect densities that create electronic states in the bandgap, which deteriorate the device performance [88]. To avoid this negative effect, numerous subsequent efforts to passivate interface defects have been made, including oxidation, nitridation, and chemical treatment [91, 92, 93]. Formation of GeO_2 between the Ge substrate and high-*k* dielectric material has been also proposed to enhance the poor interfacial characteristics of Ge-based devices since this can suppress the formation of an unintended interlayer [94].

Germanium oxides have diverse oxide phases, including GeO_2, Ge_2O_3, GeO, and Ge_2O [95]. Among these oxide phases, GeO and GeO_2 are the two representative phases of germanium oxide, and stoichiometric GeO_2 is known to be required for advanced Ge-based electronics, owing to its excellent electrical properties after formation [96]. The formation of GeO, however, is inevitable during the gate dielectric deposition or post-deposition process because of the following reactions [90]:

$$GeO_2 + Ge \rightarrow 2GeO_{(s)} \quad ,$$

$$GeO_{(s)} \rightarrow GeO_{(g)} (> 400\ ^{\circ}C) \quad .$$

The formation of undesirable GeO deteriorates the device performance since GeO in the gas phase has high reactivity as a reducing agent [97]. The reaction of gas-phase GeO with an adjacent device degrades the electrical properties of Ge-based electronics [90]. To avoid this problem, deposition of GeO_2 on a Ge substrate at a low process temperature has been proposed. There are various methods for forming GeO_2, such as thermal and chemical oxidation, and vapor deposition [98, 99, 100, 101, 102, 103]. Thermal oxidation is one of the easiest ways to synthesize an oxide film on a Ge substrate. This method ensures uniform film growth on a 3D complex Ge structure. However, as mentioned, the undesirable GeO over 400 °C is inevitable during high-temperature annealing, resulting in deterioration of the Ge-based device properties. In addition, consumption of the Ge substrate (especially channel) may result in the deterioration of device performance, wherein the device consists of nanoscale thin films such as strain-Ge and $Ge_{1-x}Sn_x$ layers [94]. Sputtering of GeO_2 can deposit stoichiometric GeO_2, but it does not satisfy the conformality and thickness controllability that modern devices require [102, 103, 104]. For these reasons, ALD has been considered as an excellent method to deposit high-quality GeO_2 at low temperatures, especially when compared with other methods. However, since there has been a lack of precursors for GeO_2 deposition to date, only a small number of reports on ALD GeO_2 have been published [94, 105, 106].

Perego et al. reported the deposition of GeO_2 layer using the ALD process for fabrication of a Ge-based metal–oxide–semiconductor (MOS) capacitor [105]. In this article, even though a systematic analysis of the growth characteristics of ALD GeO_2 is not presented, the ALD growth mode was observed using a divalent Ge precursor (1,2-bis((2,6-diisopropylphenyl)imino)acenaphthene germanium (dpp-BIAN)Ge) and an O_3 reactant. The deposited germanium oxide showed stoichiometric GeO_2 without any suboxide, and a negligible carbon impurity level. ALD-grown GeO_2 also showed an amorphous phase with extremely smooth surface roughness [0.23 nm of root-mean-square (rms) roughness]. When the dielectric property was analyzed in the fabrication of a metal–insulator–semiconductor capacitor on a Ge substrate, the dielectric constant of the ALD-grown GeO_2 was approximately 5.5, which is comparable to that of amorphous GeO_2 [107]. The band structure of the GeO_2/Ge heterojunction had been, on the other hand, investigated in order to understand the effect of a GeO_2 layer on the high-*k* semiconductor band structure using XPS. The obtained bandgap of ALD GeO_2 was approximately 5.81 eV, and the conduction band offset and valence band offset were 0.6 ± 0.1 and 4.5 ± 0.1 eV, respectively, which match with those from previous reports [108]. According to the XPS measurement, ALD GeO_2 using a divalent precursor was suggested to be a promising material for forming a passivation layer in a Ge-based device. The growth characteristics of ALD GeO_2 were first reported in an experiment using two similar tetravalent precursors:

https://doi.org/10.1557/jmr.2019.347 Published online by Cambridge University Press

© Materials Research Society 2019

bis(dimethylamino) (*N*,*N*′-diisopropyl-ethylenediamine)germanium and bis(dimethylamino) (*N*,*N*′-di-*tert*-butyl-ethylenediamine)germanium [106]. In this report, the self-limited growth behavior of ALD GeO_2 was observed as a function of precursor pulse time for the two precursors. The ALD window from 200 to 320 °C was examined for the two precursors, and in both cases, the GeO_2 film showed smooth surface roughness with negligible carbon impurities.

Only a small number of studies on ALD GeO_2 have been published, and there is a lack of systematic studies on ALD GeO_2, especially with regard to using a tetravalent precursor. Using a low-valent precursor might encourage ALD thin film growth at lower temperatures [109]; however, it might also produce a film with different phases, including understoichiometric metal oxides [110]. For the purpose of forming a stoichiometric GeO_2, a tetravalent Ge precursor could help form a stoichiometric GeO_2 more favorably than using a divalent precursor. Yoon et al. recently reported a systematic study on ALD GeO_2 using tetravalent precursors, tetrakis(dimethylamino)germanium ($Ge(NMe_2)_4$) and germanium *n*-butoxide ($Ge(OnBu)_4$), and an O_3 reactant [111]. All the film properties of ALD GeO_2 were compared with those of sputtered GeO_2. Both precursors showed self-limited growth characteristics [Fig. 3(a)], in terms of saturated growth rate and increased linear thickness, as a function of precursor exposure time and the number of ALD cycles, respectively. The saturated growth rates of ALD GeO_2 were 0.45 Å/cycle for $Ge(NMe_2)_4$ and 0.3 Å/cycle for $Ge(OnBu)_4$ at 200 °C. It was noted that the exposure time of $Ge(NMe_2)_4$ for growth rate saturation is shorter than that of $Ge(OnBu)_4$. From a density functional theory calculation, the reaction between surface hydroxyl and $Ge(NMe_2)_4$ was noted to be more thermodynamically favorable than the reaction between surface hydroxyl and $Ge(OnBu)_4$, since the bond dissociation energies of O–Ge are much larger than that of N–Ge, resulting in a more stable bond formation [112]. In addition, mobility of the molecules is inversely proportional to the molecular weight, thus the lighter $Ge(NMe_2)_4$ can be quickly attached on the substrate. Both the reactivity and mobility allow a short exposure time of $Ge(NMe_2)_4$ for surface saturation. The smaller growth rate of ALD GeO_2 using $Ge(OnBu)_4$ can be understood by the projected surface area of the adsorbed precursor species [62]. In this case, the van der Waals radius of $Ge(OnBu)_3$ (~8.5 Å) is much larger than that of $Ge(NMe_2)_4$ (~4.7 Å). Since the large size of the precursor hinders the reaction between the subsequent precursor and the surface hydroxyl species, the growth rate is, therefore, lowered. As shown in Fig. 3(b), the growth rate of ALD GeO_2 using $Ge(NMe_2)_4$ increases rapidly when the growth temperature is over 250 °C, whereas the growth rate using $Ge(OnBu)_4$ is retained from 200 to 330 °C. Because of the thermal decomposition of $Ge(NMe_2)_4$ with surface hydroxyl species, the growth rate increases rapidly, and a narrower range of process temperature can be observed than that using $Ge(OnBu)_4$.

As mentioned in the introduction of this section, deposition of stoichiometric GeO_2 is important for semiconductor applications. Stoichiometric GeO_2 was deposited with $Ge(NMe_2)_4$ and $Ge(OnBu)_4$ precursors. In the XPS measurement of ALD and sputtered germanium oxide films, the "O/Ge" ratio for ALD was approximately 1.96 for $Ge(OnBu)_4$ and approximately 1.95 for $Ge(NMe_2)_4$, whereas that of sputtered was ~1.87. This stoichiometry of ALD GeO_2 was determined based on the presence of suboxide in the GeO_2 film. From the XPS analysis, as shown in Figs. 3(c) and 3(d), Ge 3*d* and O 1*s* peaks of ALD and sputtered GeO_2 can be deconvoluted to two peaks: one is the O–Ge–O (Ge^{4+}) peak and the other is the O–Ge (Ge^{2+}) peak. Among the various Ge suboxides, germanium monoxide is known to have negative components which degrade the electrical properties of GeO_x by acting as trap sites and oxygen vacancies [113]. The presence of GeO in the GeO_2 film leads to an increase in leakage of current; thus, it is highly important to suppress the formation of GeO while depositing GeO_2. The thermally grown GeO_2 at a process temperature of over 500 °C contains a considerable amount of GeO because GeO can be transformed from GeO_2, as described in the introduction. That means GeO_2 bond can be easily transformed to GeO by external energy. Similarly, highly energetic species such as ions or radicals might induce the formation of GeO, resulting in an undesirable stoichiometric of the GeO_2 film grown by sputtering.

As described in the previous paragraph, the formation of GeO could be suppressed when the process temperature is sufficiently low. In other words, the presence of the suboxides in GeO_2 can also be presumed by the etch properties of the GeO_2 film in water since the wet etch rate of germanium oxide depends on its stoichiometry or crystallinity [90]. Figure 3(e) shows the transmittance of 50-nm-thick GeO_2 on a transparent glass substrate after 1 s of water etching. Unlike the transmittance spectra of ALD-grown GeO_2, relatively poor transmittance was observed on sputtered GeO_2. To quantify the residue after water etching of GeO_2, energy-dispersive X-ray spectrometry was used for those samples after 1 s of water etching [Fig. 3(f)]. In this experiment, a negligible Ge signal was observed for ALD-grown GeO_2 films, indicating that almost every GeO_2 was dissolved in water, whereas over 5% of Ge remained for the sputtered GeO_2 substrate. Even though the etch rates of GeO_2 grown by ALD and sputtering were similar, germanium oxide phases other than GeO_2 were not etched completely. Especially, amorphous GeO was insoluble, thus the undissolved phase of germanium oxide would remain as a noncontinuous morphology, deteriorating the transmittance of the GeO_2 film.

https://doi.org/10.1557/jmr.2019.347 Published online by Cambridge University Press

© Materials Research Society 2019

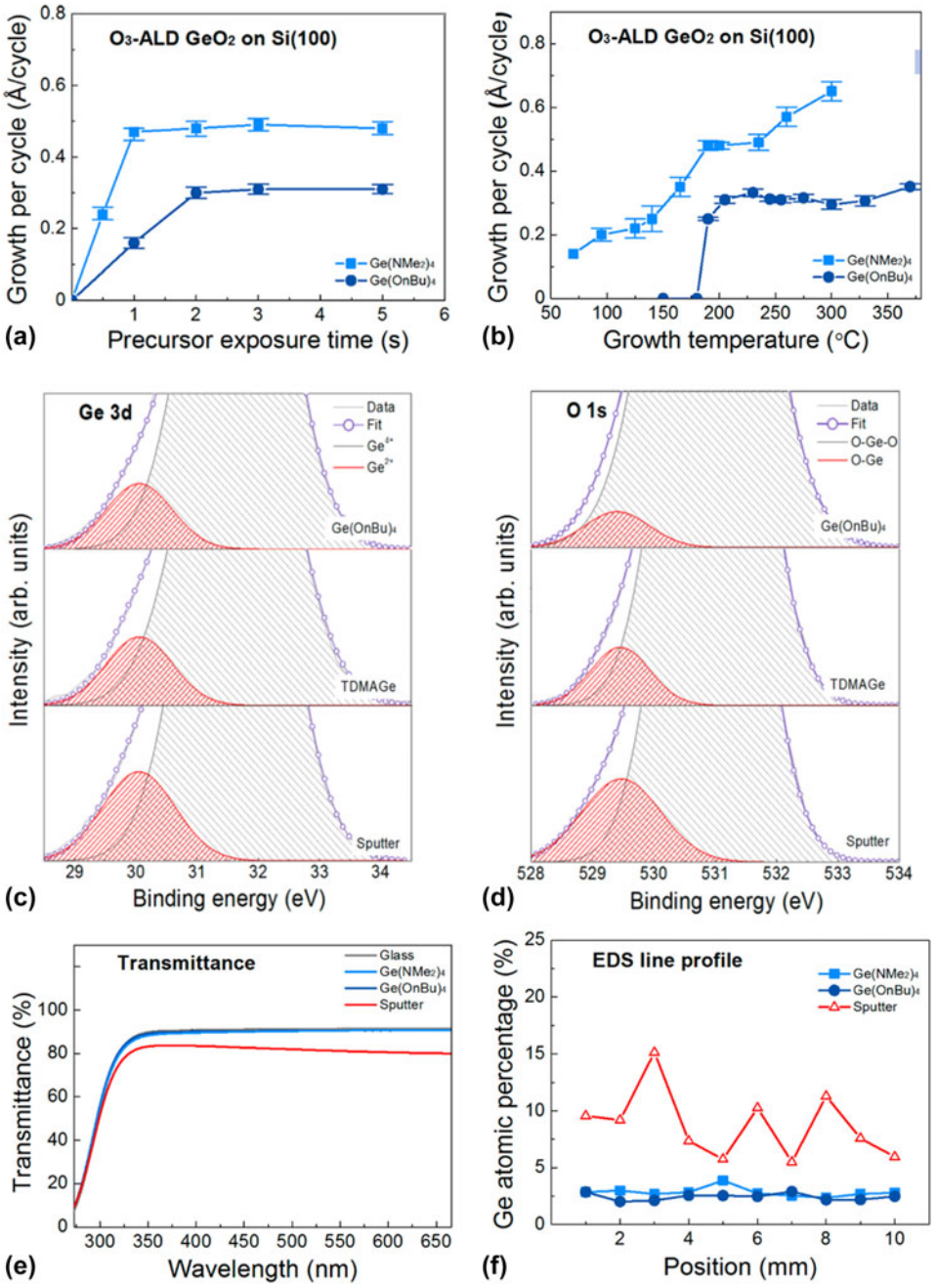


Figure 3: Growth rates of ALD GeO_2 using $Ge(NMe_2)_4$ and $Ge(OnBu)_4$ as a function of (a) precursor exposure time and (b) growth temperature, and deconvoluted XPS spectra of (c) Ge 3*d* and (d) O 1*s*. (e) Transmittance and (f) EDS line spectra of etched GeO_2 films on transparent glass. Reprinted with permission from Ref. 111. Copyright 2018 American Chemical Society.

From the microstructure analysis by X-ray diffraction (XRD), all the GeO_2 films grown by ALD and sputtering show an amorphous phase. When the mass densities of the GeO_2 film were measured by X-ray reflectivity (XRR), a relatively small density of sputtered GeO_2 (2.08 g/cm^3) was obtained when compared with that of ALD GeO_2 based on $Ge(NMe_2)_4$ (2.24 g/cm^3) or based on $Ge(OnBu)_4$ (2.35 g/cm^3). This is due to the incorporation of a large amount of GeO species in the sputtered GeO_2 film. In the case of surface roughness measured by XRR, ALD-grown GeO_2 films show smooth surface (rms roughness ~0.38 nm), whereas sputtered GeO_2 showed comparatively high roughness (approximately 2.80 nm). A similar trend on surface morphology of deposited GeO_2 was also found on roughness measurement by atomic force microscopy (AFM). The rms roughness of ALD GeO_2 by $Ge(NMe_2)_4$, $Ge(OnBu)_4$, and sputtered GeO_2 was 0.2, 0.1, and 2.9 nm,

https://doi.org/10.1557/jmr.2019.347 Published online by Cambridge University Press

© Materials Research Society 2019

respectively. Owing to the peculiar growth characteristics of ALD, the ALD-grown GeO_2 shows smooth surface compared with sputtered GeO_2.

For the electrical property evaluation of ALD GeO_2, an MOS capacitor was fabricated on the Si substrate. The thickness of ALD and sputtered GeO_2 was fixed to 10 and 30 nm, respectively. The capacitance–voltage (C–V) and current–voltage (I–V) curves are presented in Figs. 4(a) and 4(b). The C–V curves of the ALD-grown GeO_2 show typical behavior of dielectric materials on p-Si substrate with small hysteresis (~100 mV) and interface state density (D_{it}) (1.6×10^{12} and 8.3×10^{11} for ALD GeO_2 by $Ge(NMe_2)_4$ and $Ge(OnBu)_4$, respectively). The calculated dielectric constants of ALD GeO_2 by $Ge(NMe_2)_4$ and $Ge(OnBu)_4$ are 5.77 and 5.94, respectively, and these are well-matched with those that are previously reported for GeO_2 films [114]. On the other hand, in the case of the C–V curve of sputtered GeO_2, the accumulated capacitance is smaller than that of ALD GeO_2 ($k \sim 1.05$), and a large hysteresis (~2 V) and D_{it} ($\sim 9.2 \times 10^{12}$) are also observed. In an I–V analysis, the leakage current density of ALD GeO_2 is acceptable for the dielectric [$\sim 5.0 \times 10^{-7}$ and 1.7×10^{-7} A/cm^2 at −1 MV/cm for ALD GeO_2 by $Ge(NMe_2)_4$ and $Ge(OnBu)_4$, respectively], whereas sputtered GeO_2 shows poor leakage characteristics that cannot be applied to dielectric applications (4.2×10^{-2} A/cm^2). These poor electrical properties of sputtered GeO_2 originated from the formation of GeO. Germanium monoxide is known to have poor electrical properties since the Ge–O bonds act as trap sites and oxygen vacancies, leading to a high leakage current and poor C–V characteristics.

By utilizing ALD GeO_2 as a water-soluble material, ALD GeO_2 can also be applicable to the fabrication of a secure memory device. It has been demonstrated that the charge-trapping memory (CTM) that is fabricated with ALD GeO_2 as a sacrificial layer can be easily broken by simply dropping a water droplet on the device, which loses its memory property. For the fabrication of a secure memory device, 40-nm-thick ALD GeO_2 was deposited between the SiN_x/SiO_2 layer and the top ruthenium electrode as a control gate oxide using $Ge(OnBu)_4$. The device structure and the electrical properties of the CTM device before and after water etching are shown in Figs. 4(c) and 4(d). Under normal operation conditions, charges were stored inside the SiN_x layer, which is an ideal behavior for memory devices. When a single droplet of water was dropped on the device, however, the electrical properties of the CTM device were degraded, leading to the device losing its electrical information entirely.

In this section, the recent progress of ALD GeO_2 is summarized. It has been proven in the literature that ALD GeO_2 has excellent film properties that can be applied to Ge-based electronics. ALD GeO_2 using tetravalent precursors ($Ge(NMe_2)_4$ and $Ge(OnBu)_4$) shows low impurity level, negligible incorporation of suboxides such as GeO, high density, and low surface roughness. From the electrical property analysis of the MOS capacitor with ALD GeO_2, it has been found that excellent dielectric properties with a comparable dielectric constant with those grown by other methods, and low defect densities are obtained, which indicates that ALD GeO_2 is a suitable material for the fabrication of Ge-based electronics. In addition, owing to the water-soluble characteristics of the stoichiometric GeO_2 film, the material also shows the possibility for being used in the fabrication of destructive memory devices. Although the water-erasable device presented in this review is only a prototype of a future secure device, it is believed that fabrication of this device using newly developed ALD-based GeO_2 can be further advanced and lead to large-scale manufacturing.

2-Dimensional transition metal dichalcogenides

After the introduction of graphene, a 2D honeycomb structure of carbons, by Novoselov et al. [115], many researchers predicted that graphene will be a breakthrough that can overcome the current limitation of Si-based electronics, due to its remarkable electron mobility of over 10,000 cm^2/V s with just a few atomic-layer-thick flakes [116]. Despite its superior conductivity, graphene itself does not have a bandgap (E_g); thus, it cannot be used as the channel material for transistors. Instead, 2D TMDCs were the focus among promising candidate materials for future electronics from early 2010. TMDC is a type of layered 2D material with van der Waals interactions and consists of metal cores and chalcogen elements [117]. TMDCs have strong in-plane covalent bonding and weak out-of-plane van der Waals bonding, which are similar to graphene, and their film properties depend on the number of TMDC layers [118, 119]. A notable difference between graphene and TMDCs is the presence of a bandgap (E_g). Predominantly, many TMDCs (MX_2: M = Mo, W, X = S, Se, Te) exhibit semiconducting characteristics with a finite bandgap in the range of 1–2 eV [120, 121, 122]; thus, they can act as channel materials for complementary metal oxide semiconductor (CMOS) devices and other electronics. In 2011, superior electrical properties of exfoliated MoS_2 were reported for the first time in the fabrication of a field-effect transistor, showing an on/off current ratio of ~10^8 and electron mobility of over 200 cm^2/V s [123]. In addition, 2D TMDCs have been highlighted as a promising material for optoelectronic devices since they are thermodynamically and chemically stable, and they show a broad range of wavelengths for light absorption with only a couple of nanometer-thick sheets [124, 125]. Many TMDCs are predicted to show unexpected characteristics with just a couple of atomic thickness that conventional 3D

https://doi.org/10.1557/jmr.2019.347 Published online by Cambridge University Press

© Materials Research Society 2019

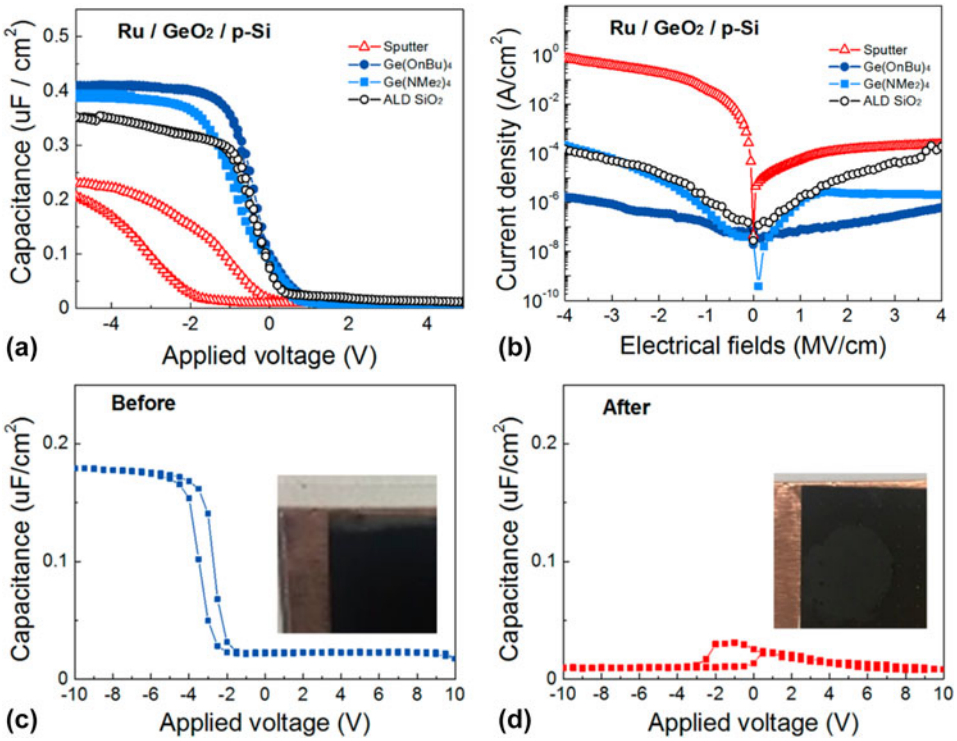


Figure 4: (a) *C–V* and (b) *I–V* curves of MOS capacitor with 10-nm-thick sputtered and ALD GeO_2 films prepared using $Ge(OnBu)_4$ and $Ge(NMe_2)_4$ with 10-nm-thick ALD SiO_2. *C–V* curves of CTM (c) before and (d) after etching by a droplet of water at RT for 1 s. Reprinted with permission from Ref. 111. Copyright 2018 American Chemical Society.

materials do not have, by numerous experiments and first principle calculations [117, 124, 126, 127, 128, 129]; thus, TMDCs have been considered a prospective material that can replace Si-based materials for electronics.

Despite the numerous advantages discussed, these materials have not been applied to mass production because of immature synthetic methods. Most of the early TMDC research focused on exfoliation from the bulk crystal because there was a lack of synthetic methods but exfoliation [123, 130]. Physical and chemical exfoliation of TMDCs are simple methods for fabricating TMDC-based devices, since the flakes that are peeled off from the bulk crystal retain the original crystal structure, which allows maintenance of the superior electrical properties of the inherent material [131]. This method, however, only allows fabrication of laboratory-scale devices due to its poor transfer yield from bulk TMDC crystals. The number of TMDC layers is also hard to control by exfoliation; that is, the various characteristics of TMDCs that are determined by the number of layers cannot be modulated as intended. Thus, it is highly desirable to synthesize 2D TMDCs with large-area uniformity and layer controllability, with methods such as solution synthesis, chalcogenization of metal oxide, and direct CVD growth [131, 132]. The direct CVD growth method is one of the fascinating methods for large-scale fabrication, which satisfies the requirement of large-area uniformity. By simultaneous exposure of metals and chalcogen precursors, TMDCs of 1–3 layers are formed on the substrate. Initially, the reacting chemical species start to form a TMDC flake with a triangular shape [133], and it continues to grow when two or more MoS_2 flake boundaries meet. Despite this facile way for MoS_2 synthesis, a much improved wafer-scale uniformity and precise layer controllability by CVD are still challenging for large-scale device fabrication. In addition, the characteristics of TMDCs are poorer than those of mechanically exfoliated TMDCs because of the numerous grain boundaries that are generated during synthesis [117]. In terms of these requirements, ALD is a promising method for 2D TMDC synthesis, since it can overcome these limitations owing to its peculiar deposition mechanism.

Synthesis of 2D TMDCs (WS_2 and MoS_2) by sulfurization of ALD-grown metal oxides

The initial research on ALD-based TMDC growth began with the chalcogenization of metal oxide that was deposited by ALD. In 2013, Song et al. reported WS_2 nanosheet synthesis by sulfurization of ALD-grown WO_3 [134]. WS_2 is one of the TMDCs that has been widely studied owing to its peculiar characteristics, including electrical [135, 136], optical [137, 138, 139], magnetic [140, 141], and even catalytic properties [142,

https://doi.org/10.1557/jmr.2019.347 Published online by Cambridge University Press

© Materials Research Society 2019

143]. Despite these notable properties, there has been a lack of research on the synthesis of WS_2 with excellent thickness controllability and large-area uniformity. In terms of layer controllability, however, sulfurization of ALD-grown oxide can easily overcome the limitations by controlling the thickness of the metal oxide before sulfurization. For the deposition of WO_3, bis(isopropylcyclopentadienyl)tungsten(IV) dihydride ($WH_2(iPrCp)_2$) was used as a W precursor and O_2 plasma as a reactant. Sulfurization of a WO_3 film into WS_2 nanosheets was conducted with S powder at 1000 °C for 30 min. The number of WS_2 layers was easily controlled from monolayer to multilayers by changing the thickness of ALD-grown WO_3. ALD WO_3 films, grown over 20, 30, and 50 ALD cycles, were sulfurized at 1000 °C for 30 min, and those films were entirely transformed to nanosheets of 1, 1.6, and 3 nm, respectively, which correspond to the mono-, bi-, and tetra-layer of WS_2 [Figs. 5(a)–5(c)]. The number of layers is estimated by the spacing between WS_2 layers or the WS_2 and SiO_2 substrate. The spacing between WS_2 and SiO_2 is typically known to be 1 nm, and between WS_2 layers is 0.6 nm, which are in good agreement with the estimated number of layers of sulfurized WS_2 [144].

Raman spectroscopy and photoluminescence (PL) that are shown in Figs. 5(d)–5(f) were used to distinguish the number of WS_2 layers. In Raman spectroscopy, two clear peaks from in-plane and out-of-plane vibration of WS_2 were observed at approximately 356 and 420 cm^{-1} for mono-, bi-, and tetra-layers of WS_2. As the number of WS_2 layers increases, two notable changes can be observed, which are the peak intensity ratio of E^1_{2g} and A_{1g}, and the peak distance between them, as shown in Fig. 5(e). As the number of WS_2 layers increases from mono- to tetra-layer, the peak intensity ratio increases because the Raman intensity is mainly affected by the scattering volume of WS_2 [145]. The peak distance between E^1_{2g} and A_{1g} also increases as the number of WS_2 layers increases, owing to the weak interlayer interaction and reduced long-range Coulomb interaction between the effective charges in WS_2 layers that originated by an increase in the dielectric screening [133, 146]. From a PL analysis, as shown in Fig. 5(d), a strong signal of monolayer WS_2 can be observed at 2.01 eV, which corresponds to the reported E_g of the WS_2 monolayer. However, only weak signals can be observed at 1.97 eV for bilayer WS_2, and 1.4 eV for the tetra-layer. This phenomenon is originated by direct to indirect E_g transition of 2D TMDCs, which closely matched with previous reports [121, 144]. The stoichiometry of the WS_2 layer was confirmed by quantitative analysis using XPS, in which the calculated ratio of W and S was 2, indicating that sulfurization of WO_3 at 1000 °C can form a stoichiometric WS_2 [147]. In high-resolution transmission electron microscopy (HRTEM) analysis, the WS_2 nanosheet that was transferred onto the TEM grid shows periodically arranged atoms, and the selected area electron diffraction (SAED) pattern [as shown in the inset of Fig. 5(g)] also shows the polycrystalline (100) and (110) phase of WS_2, in which the grain size is approximately 10–20 nm. The grain size of WS_2 is comparable to that of the MoS_2 nanosheet synthesized by Mo sulfurization [148].

ALD-based TMDC synthesis satisfies the requirements of large-area uniformity and excellent conformality for film deposition. These requirements are prerequisites for large-scale device fabrication, owing to the peculiar growth characteristics and self-limiting growth manner that can be expected from satisfying these requirements. ALD-based WS_2 synthesis also showed wafer-scale uniformity up to 6 inches [Fig. 5(h)]. In addition, in terms of excellent conformality of ALD, WS_2 nanotubes were well synthesized by forming WS_2 on SiO_2/Si nanowire, followed by etching with HF [Fig. 5(i)]. By using ALD-based WS_2 synthesis, not only the number of WS_2 layers but also the diameter or even the length of the nanotube can be modulated, which cannot be achieved by other methods. From the electrical property characterization of ALD-based WS_2 by fabrication of a field-effect transistor (FET) [Fig. 5(j) for the transfer curve of monolayer WS_2-FET], the electron mobility and sub-threshold swing (SS) were 3.9 cm^2/V s and 0.6 V/dec, respectively. In particular, the electron mobility was much higher than that of WS_2 FETs that had been previously reported due to the suppression of charged impurity scattering by deposition of high-*k* dielectric, also known as the dielectric screening effect [123, 149, 150].

MoS_2, one of the well-known 2D TMDCs owing to its superior electrical and optical properties [123, 151, 152], was also synthesized using the chalcogenization method. In 2015, Song et al. reported a synthetic method for MoS_2 using sulfurization of ALD-grown MoO_x [153]. In this report, MoO_x was grown on a SiO_2/Si substrate using $Mo(CO)_6$ as a precursor and O_2 plasma as a reactant at 200 °C. As shown in Fig. 6(a), the MoS_2 that was synthesized using one-step sulfurization, which was also previously used for WS_2 synthesis [134], showed numerous granular-like particles on top of the surface, which was formed by the vaporization of MoO_x that occurred at approximately 700 °C [154]. Since this rough surface was not suitable for smooth TMDC synthesis, two-step sulfurization was applied to avoid the vaporization of ALD MoO_x. For two-step sulfurization, ALD MoO_x was initially sulfurized at 600 °C for 60 min, which can avoid the vaporization of MoO_x, and the process temperature was then increased to 1000 °C and maintained for 30 min. MoS_2 that was synthesized using two-step sulfurization shows a smooth surface, compared with that of MoS_2 that is synthesized by one-step sulfurization. Similarly, Keller reported the synthesis of MoS_2 by sulfurization of an ALD-grown MoO_x film using a bis(*tert*-butylimido) bis(dimethylamido)molybdenum [$(tBuN)_2(NMe_2)_2Mo$] precursor [155], and a similar granular-like nucleation was

https://doi.org/10.1557/jmr.2019.347 Published online by Cambridge University Press

© Materials Research Society 2019

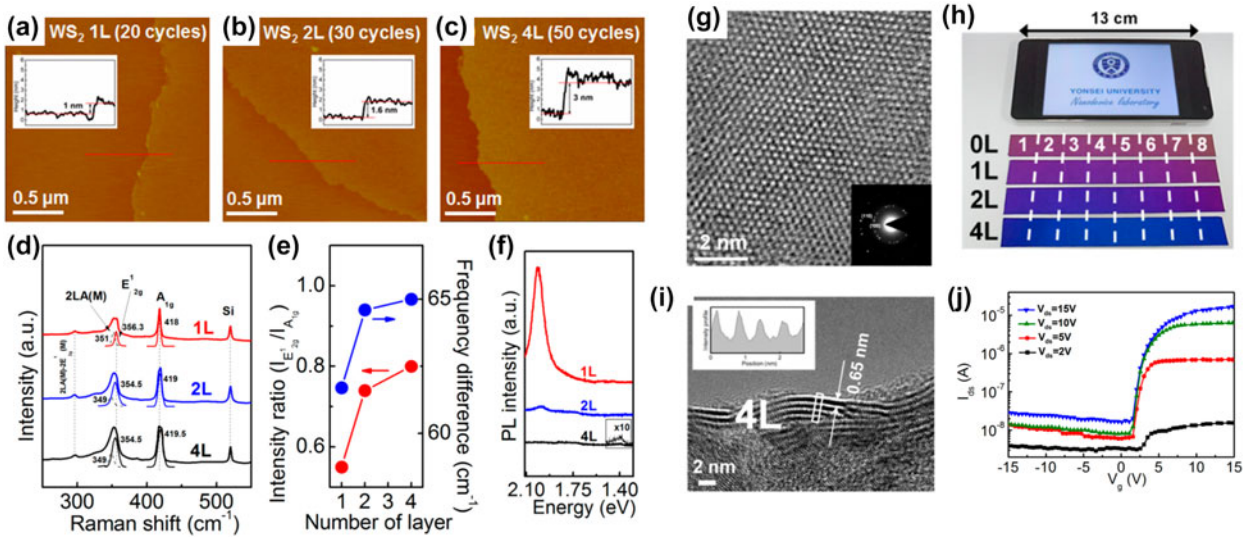


Figure 5: AFM images and height profiles (inset) of the transferred WS_2 nanosheet on the SiO_2 substrate for the (a) mono-, (b) bi-, and (c) tetra-layered thicknesses, respectively. (d) Raman spectra for the mono-, bi-, tetra-layer WS_2 nanosheets on SiO_2, and (e) relative Raman peak intensities and peak distances of the E^1_{2g} and A_{1g} bands for the WS_2 layers. (f) PL spectra for the WS_2 nanosheets. (g) HRTEM image of the monolayer WS_2 nanosheet, and (h) large area uniformity (approximately 13 cm) of WS_2 nanosheet on SiO_2 substrate. (i) HRTEM image of the tetra-layer WNT and (inset) the intensity profile of the region denoted by the solid line. (j) Electrical properties of the monolayer WS_2 nanosheet by fabrication of FET. Reprinted with permission from Ref. 134. Copyright 2013 American Chemical Society.

observed after the sulfurization of MoO_x. In this article, the granular nature of the synthesized MoS_2 was caused by the morphology of precursor oxide formed and could be solved through pretreatment methods, such as piranha cleaning, to increase the density of surface hydroxyl, resulting in a smooth growth of precursor oxide on the substrate. The number of MoS_2 layers was controlled by changing the thickness of the MoO_x, as shown in Fig. 6(b). In this experiment, 6, 9, and 12 cycles of ALD MoO_x were entirely transformed to 1, 1.6, and 2.3 nm of MoS_2, which correspond to the mono-, bi-, and tri-layer of MoS_2, respectively [118, 130]. Raman and PL spectra of MoS_2 grown using ALD MoO_x showed that the Raman peak distance between E^1_{2g} and A_{1g} increased as the number of layers increases and the strong PL peak for the monolayer MoS_2 disappeared when the number of MoS_2 layers increased. These patterns are the same as those observed for WS_2, as described in the previous paragraph.

Synthesis of $Mo_{1-x}W_xS_2$ by sulfurization of ALD-grown $Mo_{1-x}W_xO_y$

The focus of bandgap modulation of 2D TMDCs was mainly on the performance enhancement of optoelectronic devices, such as photodiode or phototransistor [156, 157], because of its superior light absorption characteristics in a couple of nanometer-thick TMDC sheets. Even though the E_g of TMDCs can be modulated by changing the number of layers, alloying two different TMDCs with different E_g can tune the E_g of TMDCs with great flexibility and access an almost continuous light absorption range [158, 159]. One of the notable differences of ALD among various deposition methods is that ALD enables a precise control of composition of the film by intermixing two different ALD processes in a single ALD step. This method is called supercycle and is frequently used for doping or alloy ratio control of ternary or quaternary compounds [18, 22, 160, 161, 162, 163, 164]. Hence, alloys of 2D TMDCs can be formed by sulfurization of alloyed metal oxides in which composition is precisely controlled by the ALD supercycle.

Based on the synthesis of MoS_2 and WS_2 that are introduced in the section "Synthesis of 2D TMDCs (WS_2, MoS_2) by sulfurization of ALD-grown metal oxides," $Mo_{1-x}W_xS_2$ alloys were synthesized by sulfurization of $Mo_{1-x}W_xO_y$ alloy grown by an ALD supercycle [153]. The composition of $Mo_{1-x}W_xO_y$ was easily controlled by changing the number of ALD cycles in a single ALD supercycle, and systematic modulation of $Mo_{1-x}W_xS_2$ composition was confirmed by XPS quantification analysis. As shown in Fig. 7(a), synthesized $Mo_{1-x}W_xS_2$ alloys that were sulfurized by a single supercycle of $Mo_{1-x}W_xO_y$ show 1 nm of thickness regardless of the alloy ratio, which is the thickness of a single layer of $Mo_{1-x}W_xS_2$. That is, two or more layers of $Mo_{1-x}W_xS_2$ can be synthesized by increasing the number of $Mo_{1-x}W_xO_y$ supercycle, allowing excellent layer controllability of $Mo_{1-x}W_xS_2$. The intermix of $Mo_{1-x}W_xS_2$ was confirmed by Raman spectroscopy, PL, and XPS analysis. In particular, the notable shift of PL peaks intended was observed, which was depending on their composition ratios. As shown in Figs. 7(b) and 7(c), the peak

https://doi.org/10.1557/jmr.2019.347 Published online by Cambridge University Press

© Materials Research Society 2019

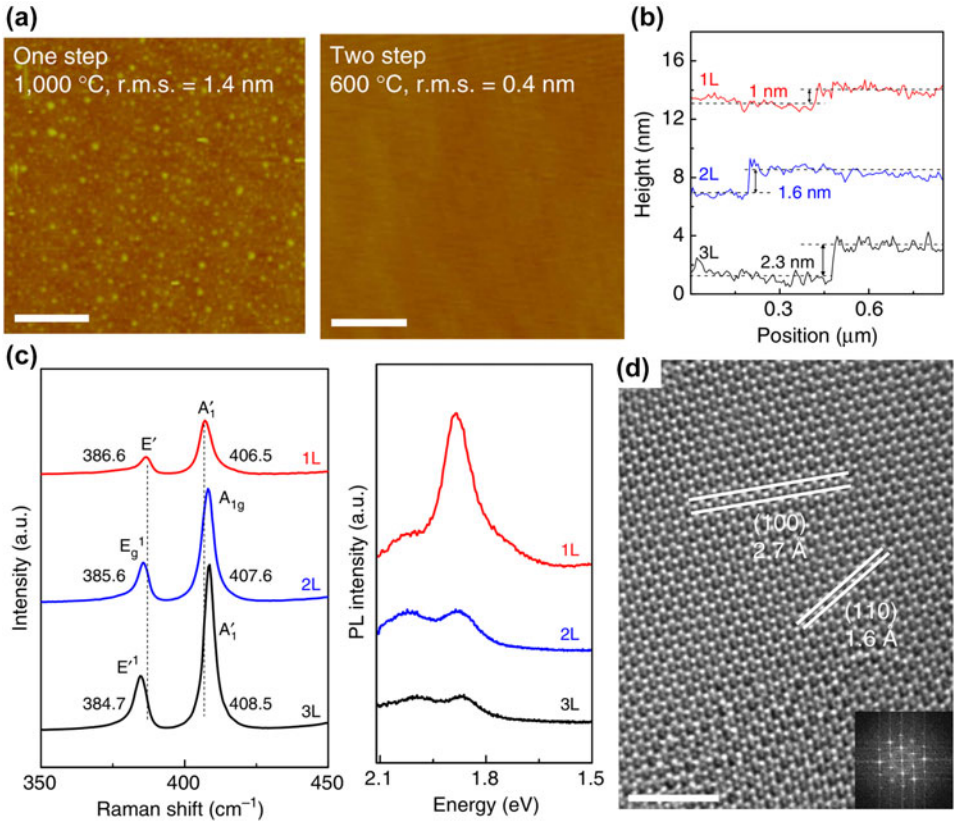


Figure 6: (a) AFM images of sulfurized MoO_x thin film using one-step sulfurization at 1000 °C and two-step sulfurization at first-sulfurization temperature of 600 °C. (b) Height profiles of transferred MoS_2 on SiO_2 substrate for mono-, bi-, and trilayer thickness. (c) Raman and PL spectra, and (d) HR-TEM image of MoS_2 and (inset) FFT pattern [153].

position of the $Mo_{1-x}W_xS_2$ alloy from the PL spectra shows generally a gradual increase in the PL peak position as the amount of W in the alloy increases, except for the $Mo_{0.7}W_{0.3}S_2$ sample, which is due to the bowing effect that has been observed in many semiconductor alloys [165, 166].

Vertically composition-controlled (VCC) $Mo_{1-x}W_xS_2$, which has been highlighted in high-performance optoelectronics owing to its interlayer functionality, such as interlayer transition, was also synthesized by sulfurization of a VCC $Mo_{1-x}W_xO_y$ film [167, 168]. Prior to sulfurization, the VCC $Mo_{1-x}W_xO_y$ film was deposited with 5 ALD supercycles at different ALD cycle ratios. Initially, 20 cycles of ALD WO_3 were conducted on a SiO_2 substrate, which correspond to growing a monolayer of WS_2. Three supercycles with different ALD cycle ratios were sequentially conducted, from WO_3-rich to MoO_x-rich alloys. Each supercycle with a different ALD cycle ratio was consistent with a monolayer of $Mo_{1-x}W_xS_2$ alloy. Finally, 3 cycles of ALD MoO_x, which correspond to a MoS_2 monolayer, were conducted. After sulfurization of VCC $Mo_{1-x}W_xO_y$, AFM measurement of VCC $Mo_{1-x}W_xS_2$ confirmed that 5 layers of the TMDC alloy were synthesized by sulfurization of 5 sequential ALD supercycles (approximately 3.5 nm). Moreover, angle-resolved XPS (ARXPS) and Raman peak distance results [as shown in Figs. 7(d) and 7(e)] showed that atomic concentration of VCC $Mo_{1-x}W_xS_2$ was gradually changed from the lowermost layer to the uppermost layer, demonstrating the synthesis of $Mo_{1-x}W_xS_2$ alloy with controlled composition based on the ALD process.

With this VCC $Mo_{1-x}W_xS_2$ method, not only the composition controllability but also an additional effect from interlayer couplings, for instance, interlayer transitions, can be obtained [169, 170]. Compared with the VCC $Mo_{1-x}W_xS_2$ that were stacked by the transfer method of each differently composed $Mo_{1-x}W_xS_2$ alloy, greater light absorption was obtained for VCC $Mo_{1-x}W_xS_2$ synthesized by sulfurization of $Mo_{1-x}W_xO_y$ with ultraviolet-visible (UV-Vis) spectroscopy, owing to its strong interlayer coupling that cannot be obtained by other methods. When the light absorption spectrum of VCC $Mo_{1-x}W_xS_2$ that are stacked was subtracted from that of VCC $Mo_{1-x}W_xS_2$ synthesized by sulfurization, a small absorbance peak was observed at 1.87 eV, which was formed by a strong interlayer coupling. In addition, the incorporation of contaminants, including H_2O or organic compounds, can be avoided by using this ALD-based VCC $Mo_{1-x}W_xS_2$ synthesis [171]. Since the VCC $Mo_{1-x}W_xS_2$ exhibited superior light absorption in a wide range of wavelengths, as well as strong interlayer

https://doi.org/10.1557/jmr.2019.347 Published online by Cambridge University Press

© Materials Research Society 2019

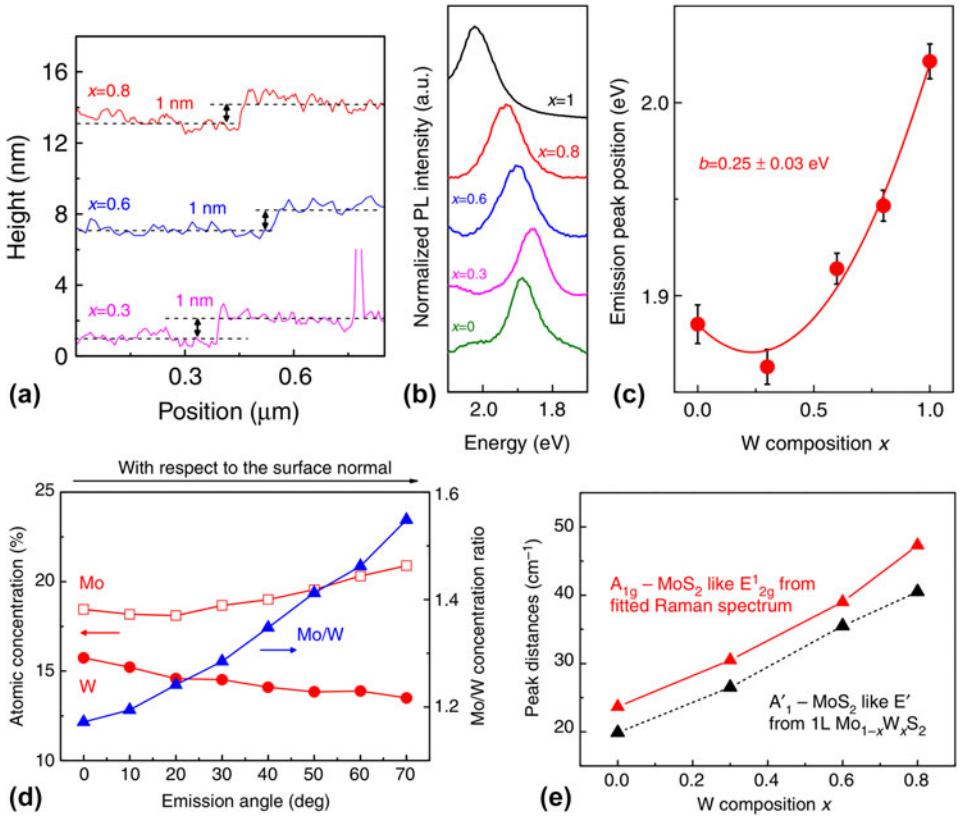


Figure 7: (a) Height profiles of transferred $Mo_{1-x}W_xS_2$ alloys on SiO_2 substrate. (b) PL spectra of monolayer $Mo_{1-x}W_xS_2$ alloys and (c) the PL peak position versus W composition. (d) Calculated atomic concentration of $Mo_{1-x}W_xS_2$ from ARXPS as a function of emission angle, and (e) calculated Raman peak distances between A_{1g} and E^1_{2g} from $Mo_{1-x}W_xS_2$ alloys [153].

coupling, 5 layers of VCC $Mo_{1-x}W_xS_2$ alloy were utilized as the active layer of the photodetector. Compared with photodetectors that were fabricated with 5 layers of MoS_2 or WS_2, the VCC $Mo_{1-x}W_xS_2$–based photodetector generated a broadband of photo-induced current from 1.2 to 2.5 eV, whereas MoS_2– or WS_2-based photodetectors generated a narrower photocurrent, from 1.3 to 2.1 eV for the WS_2 photodetector and from 1.2 to 1.8 eV for the MoS_2 photodetector. Furthermore, when white light was applied to the photodetectors, the $Mo_{1-x}W_xS_2$–based photodetector showed 3 and 4 times higher photocurrent than those of WS_2 and MoS_2, respectively, which was attributed to broadband light absorption of VCC $Mo_{1-x}W_xS_2$. These results demonstrated that VCC $Mo_{1-x}W_xS_2$ is a promising material for advanced optoelectronic applications.

Direct synthesis of 2D TMDCs by ALD

Even though the sulfurization of ALD-grown metal oxides using ALD is advantageous, this two-step process requires an additional sulfurization process as compared to the direct ALD process, which can be used to synthesize TMDCs with one step. The complexity of the process leads to an increase in cost, and sulfurization results in poor crystalline quality and small domain size, which may deteriorate the electrical properties of TMDCs [172]. Hence, it is highly desirable to synthesize TMDCs with the direct ALD process. In 2014, L. Tan reported a direct synthesis of ALD MoS_2 at 300 °C using $MoCl_5$ and H_2S as a precursor and reactant, respectively [173]. AFM and TEM analyses confirmed the exact thickness controllability of MoS_2, which indicated that conventional ALD growth of MoS_2 was obtained. Moreover, the crystallinity of MoS_2 was increased by using post-deposition annealing with sulfur vapor at 800 °C, which led to the recrystallization of MoS_2 at high annealing temperature. Furthermore, Jurca et al. reported a low-temperature growth of ALD MoS_2 using a metal–organic precursor, tetrakis(dimethylamido)molybdenum [174]. In contrast to a halide precursor, the metal–organic precursor enabled the low-temperature growth of ALD TMDC owing to its high reactivity with oxidants. Moreover, the use of the metal–organic precursor prevented a deleterious effect of by-products that could be generated after the reaction between a halide precursor and a reactant (e.g., HCl). Similarly previous reports described the conventional ALD growth of MoS_2 [175, 176, 177, 178]; however, when the process temperature was sufficiently high, the growth mechanism of direct ALD TMDCs was significantly altered. In 2016, Kim et al. reported direct

https://doi.org/10.1557/jmr.2019.347 Published online by Cambridge University Press

© Materials Research Society 2019

ALD synthesis of MoS_2 and WSe_2 using $MoCl_5$ and WCl_6 as precursors, and H_2S and diethyl selenide (DESe) as reactants [179, 180]. A notable feature of direct ALD synthesis of TMDCs using these precursors at over 500 °C is that the number of TMDC layers is determined by process temperature, not the number of ALD cycles. As shown in Figs. 8(a) and 8(b), the peak distance between A_{1g} and E^1_{2g} of ALD-synthesized MoS_2, and also the thickness of WSe_2, are saturated even when the number of ALD cycles increases, which indicates that this sequential exposure of the precursor and reactants does not show a conventional ALD growth manner. Instead, a thicker TMDC layer was obtained at a lower temperature for the synthesis of both TMDCs. For instance, as shown in Fig. 8(c), tri-layer MoS_2 (approximately 2 nm) was synthesized when the process temperature was 500 °C, while the process temperature increased to 700 and 900 °C, bi- (approximately 1.4 nm) and mono-layer MoS_2 (approximately 0.8 nm) were obtained. This peculiar phenomenon, known as the "self-limiting layer synthesis" (SLS), is considered to be caused by the inherent chemical inactivity of the TMDCs' surface [181]. When the first layer of ALD TMDC is formed on the substrate, there is a lack of precursor chemisorption site on the initially formed TMDC layer because of its chemical inactivity [182]. Only a physisorbed precursor on the TMDC layers could react with subsequent reactants. However, when the process temperature is high enough, the physisorbed chemical species are easily detached from the TMDC layer; thus, the synthesis of a TMDC layer as a function of ALD cycle is hindered [181]. Furthermore, the surface potential that was induced by the positive charge between MoS_2 and SiO_2 substrates helps to adhere the precursor on the MoS_2 substrate physically, and this potential would decrease when the number of layers increases, which would then increase the distance between the physisorbed precursor molecule and the interfacial charge [183]. It has been observed that the peak distance increased between E^1_{2g} and A_{1g} when the Raman analysis and PL signal intensity decreased in a SLS-grown MoS_2, which occurred as the number of layers increased. This is similar to the pattern observed in sulfurized MoS_2, as discussed in the previous section. The intensity ratio of E^1_{2g} and A_{1g} of WSe_2 obtained from Raman analysis also decreased when the number of layers increased.

Both MoS_2 and WSe_2 grown by the SLS method showed wafer-scale large-area uniformity up to 1.5×8 cm^2, as shown in Fig. 8(c), in which the size is limited by the reactor design. In the TEM analysis, SLS-grown monolayer MoS_2 and tri-layer WSe_2 showed excellent layer uniformity of over 95 and 90%, respectively, and both TMDCs have (100) and (110) planes of crystallinity. The electrical properties of monolayer SLS-grown MoS_2 were characterized by FET fabrication and showed n-type behavior with 0.2 cm^2/V s of field-effect electron mobility in the linear regime, 10^8 of on/off current ratio, and 0.36 V/dec of SS, which are comparable to those of single-crystal MoS_2 [123, 183]. In the case of tri-layer SLS-grown WSe_2, the material exhibited p-type characteristics with 2.2 cm^2/V s of field-effect hole mobility and 10^6 of on/off current ratio, which are significantly higher than those previously reported for WSe_2 grown with the CVD method [184].

Since the MoS_2 growth using the $MoCl_5$ precursor depends critically on the underlying substrate due to physisorption of the precursor, this SLS method can be applied to the synthesis of heterostructure of 2D TMDCs with precise layer controllability, which is challenging for conventional methods [185]. The MoS_2/WSe_2 heterostructure was fabricated by synthesizing SLS-grown MoS_2 at 800 °C on the exfoliated WSe_2 flakes on a SiO_2/Si substrate. In the Raman spectra shown in Fig. 9(a), MoS_2-related peaks (E^1_{2g} and A_{1g}) are observed only on the SiO_2 and bilayer WSe_2, not on the 12-layer WSe_2, which indicates the monolayer MoS_2 was only formed on the SiO_2 and bilayer WSe_2, not on the 12-layer WSe_2. This was also confirmed from the Raman mapping for MoS_2 E^1_{2g} peak intensity and position, shown in Fig. 9(b). In the mapping images, the MoS_2-related peak is only observed on the bare SiO_2 and 2 L of WSe_2, not on the bulky WSe_2 layers. As discussed, the synthesis of SLS-grown MoS_2 was inhibited on the 12-layer WSe_2 because of the lack of force for the precursor molecules to physisorb on top of the WSe_2 layer. In addition, there was no intermixing of MoS_2 and WSe_2 during the synthesis, as evidenced by the fact that no Raman peak related to $MoSe_2$ or WSe_2 was observed. Using this method for heterostructure fabrication, which enables precise layer control of MoS_2 on 2D TMDCs, a high-performance PN diode was also fabricated [optical microscopy image of the PN diode is shown in Fig. 9(c)]. The diode showed gate-tunable rectifying characteristics, which was explained by the variation in carrier density with electrical doping [186]. From the PL spectra, the PN diode exhibited a strong PL quenching and photovoltaic effect because of a rapid carrier separation at the junction of MoS_2/WSe_2 [187, 188]. As shown in Figs. 9(d) and 9(e), the *I*–*V* characteristics of the MoS_2/WSe_2 PN diode at gate voltage (V_g) = −50 V showed an excellent photoresponsivity of 33 mA/W at drain-source voltage (V_{ds}) = 1 V with an open circuit voltage (V_{oc}) of 0.2 V.

However, as mentioned in the first part of this chapter, not every synthesis of TMDCs using ALD shows SLS behavior, which depends on the process temperature. Recently, Kim et al. reported a conventional ALD growth of MoS_2 using MoF_6 and H_2S [189]. Unlike the synthesis of MoS_2 using $MoCl_5$, the number of MoS_2 layer synthesized by using the MoF_6 precursor was linearly increased with the number of ALD cycles. As shown in Figs. 10(a) and 10(b), the thickness of ALD MoS_2 grown at 700 °C, with 30, 60, 90, 120, and 150 ALD cycles, was 0.8, 1.5, 2.1, 2.8, and 3.3 nm, respectively. These correspond to

https://doi.org/10.1557/jmr.2019.347 Published online by Cambridge University Press

© Materials Research Society 2019

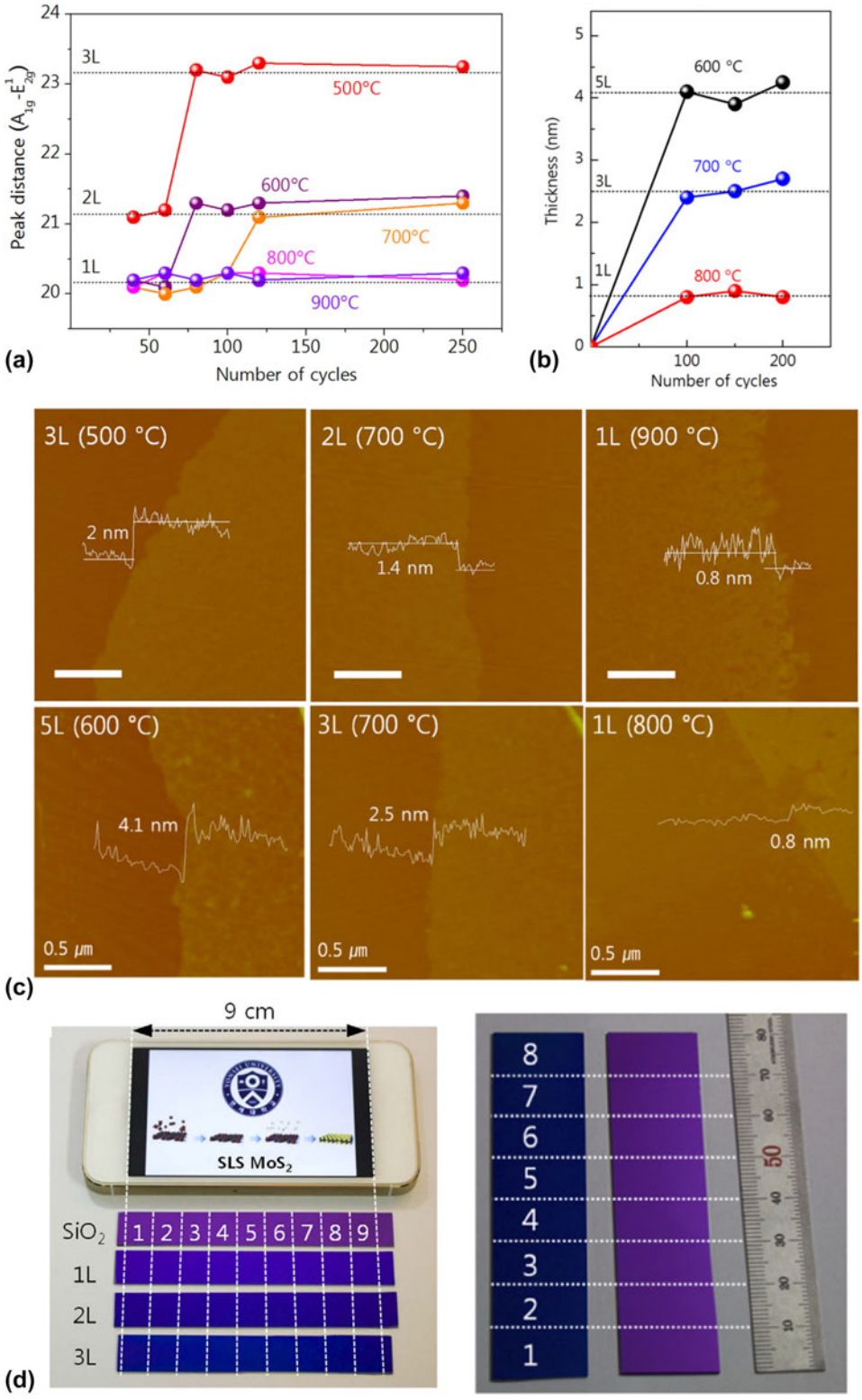


Figure 8: (a) Raman peak distance of MoS_2 and (b) thickness of WSe_2 measured by AFM as a function of process temperature. (c) AFM images of MoS_2 and WSe_2 depending on the process temperature and large-area uniformity of MoS_2 and WS_2 [179]. Reprinted with permission from Ref. 180. Copyright 2016 IOP Publishing.

the linear increase of MoS_2 from the monolayer to 5 layers. The Raman analysis and PL spectra of ALD MoS_2 using MoF_6 also showed a positional change of E^1_{2g} and A_{1g}, and the intensity decreased as a function of the MoS_2 layer, as shown in Figs. 10(c) and 10(d), which matched the results discussed in the previous section. This different growth behavior between

https://doi.org/10.1557/jmr.2019.347 Published online by Cambridge University Press

© Materials Research Society 2019

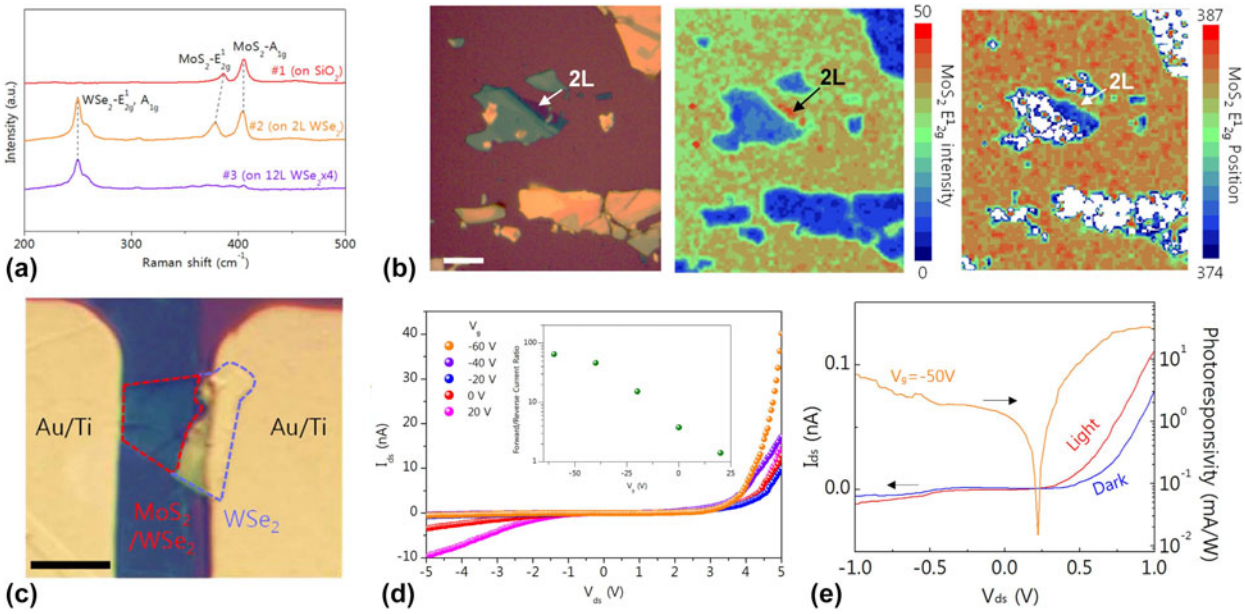


Figure 9: (a) Raman spectra of SLS MoS_2 on SiO_2, bilayer WSe_2, and 12-layer WSe_2, and (b) optical microscope image and Raman mapping for MoS_2 $E^1{}_{2g}$ peak intensity and position. (c) Optical microscope image of a MoS_2/WSe_2 heterostructure PN diode, and (d) *I–V* characteristics of the PN diode with various gate biases (inset: forward/reverse current ratio at $V_{ds} = |5\ V|$), and (e) with and without light illumination, and calculated photoresponsivity [179].

ALD MoS_2 and SLS MoS_2 might be caused by the precursors that were used for the TMDC synthesis. In this article, the exact mechanism was not clarified, but it was presumed to have originated from different chemical interactions between the precursors and the MoS_2 layer. The relatively strong binding energy between MoF_6 and the uppermost MoS_2 layer may possibly enable a reaction with the following reactants, whereas the relatively low binding energy between $MoCl_4$ and MoS_2 led to insufficient adsorption of $MoCl_4$ on MoS_2, resulting in a self-limiting growth behavior [190]. In the XPS analysis and TEM analysis, high-quality crystalline MoS_2 with (100) and (110) planes was synthesized using a MoF_6 precursor with negligible F impurities. The electrical properties of ALD MoS_2 that were evaluated by the FET [Fig. 10(e)] were n-type behavior with 0.1 cm^2/V s of electron mobility, 3.5 V/dec of SS, and 10^6 of on/off current ratio, which are comparable to those of ALD MoS_2 with a $MoCl_5$ precursor [179].

ALD MoS_2 using MoF_6 was also adopted for the fabrication of heterostructure with graphene and other TMDCs, WSe_2 in this article. When ALD MoS_2 was deposited on the CVD-grown graphene layer, the growth of monolayer MoS_2 was confirmed when the number of ALD cycles was 60 by Raman analysis [Fig. 10(f)]. After the synthesis of MoS_2 on graphene, 30 cycles of ALD were required for the additional MoS_2 layer synthesis on the MoS_2/graphene heterostructure. The longer ALD cycle for the synthesis of MoS_2 on graphene was caused by the chemical inertness of the graphene layer, which requires longer nucleation delay than that on the SiO_2 substrate [191]. In the case of MoS_2 synthesis on graphene using the $MoCl_5$ precursor, which was abbreviated as SLS MoS_2 in the previous paragraph, no MoS_2 growth on graphene was observed even after 150 cycles of ALD, indicating that MoF_6 is a suitable precursor for synthesizing MoS_2 on carbon-based 2D materials. By utilizing this MoS_2/graphene heterostructure, they fabricated an excellent photodetector without external gate voltage in operation, demonstrating the suitability of the MoS_2/graphene heterostructure for optoelectronic devices.

In the case of ALD MoS_2 on WSe_2 using MoF_6, the growth behavior was different from that on graphene. In the Raman spectra, as shown in Fig. 10(g), WSe_2 peaks disappeared after 30 cycles of ALD MoS_2 using MoF_6 and H_2S at 700 °C, indicating an etching of the WSe_2 layer during the ALD process. The Raman peaks of WSe_2 clearly disappeared after MoF_6 exposure for 1 min at 700 °C, whereas high-temperature sulfurization using H_2S showed no etching of the WSe_2 layer until 1100 °C [192], indicating that MoF_6 etched the underlying WSe_2 layer at 700 °C. Thus, ALD MoS_2 using MoF_6 is not suitable for synthesizing a heterostructure with other TMDC materials, thus indicating that further research on ALD TMDCs with various precursors should be conducted.

In this section, synthesis and characterization of 2D TMDCs by using ALD are discussed. Because of their inherently superior characteristics, the development of TMDC synthesis is expected to lead to a breakthrough in electronics, enabling the fabrication of next-generation nanoscale devices, such as neuromorphic computing devices [36]. Among various synthetic methods, ALD-based 2D TMDC syntheses, including chalcogenization of ALD-grown metal oxides and direct ALD

https://doi.org/10.1557/jmr.2019.347 Published online by Cambridge University Press

© Materials Research Society 2019

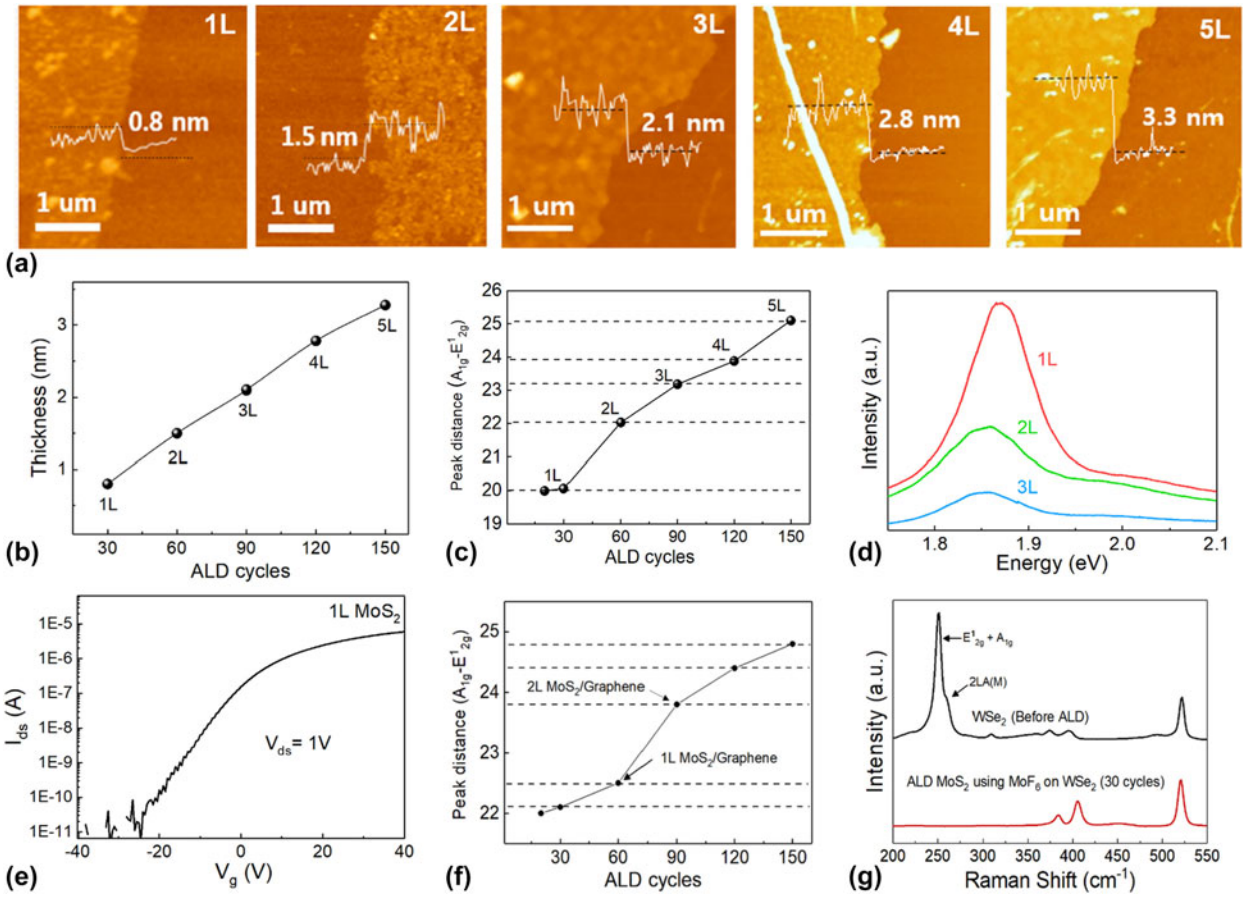


Figure 10: Atomic layer deposition of MoS_2 using MoF_6 precursor. (a) AFM images and height profiles of transferred ALD MoS_2 on SiO_2 substrate as a function of growth cycle (30, 60, 90, 120, and 150 cycles, respectively), and (b) the thickness of ALD MoS_2 measured by AFM. (c) Raman peak distance of ALD MoS_2 versus ALD cycles. (d) PL spectra of mono-, bi-, and trilayer of MoS_2. (e) Transfer curve of monolayer MoS_2 FET. (f) Raman peak distance of MoS_2/graphene versus ALD cycles. (g) Raman spectra of WSe_2 before and after the ALD MoS_2 using MoF_6. Reprinted from Ref. 189 with permission from Elsevier.

synthesis, have several advantages, including large-area uniformity and excellent layer controllability, which are prerequisites for mass production. In addition, the electrical and optical properties of TMDC nanosheets could be easily modulated by simply changing the composition ratio of TMDC by the ALD supercycle method. Despite these advantages, further research should be conducted for improvement in the properties of ALD-grown 2D TMDCs, to an extent that is comparable to exfoliated TMDCs. Furthermore, systematic investigation on the dependence of different deposition mechanisms of 2D TMDCs on precursors is also required. Through these efforts on the synthesis of 2D TMDCs by ALD, great advances in electronics and optoelectronics can be expected in the near future.

Conclusion & outlook

As discussed in this review, a rise of nonconventional materials using ALD can change the current paradigm of electronics, owing to their great potential to be universally applied. The versatility and unique properties of ALD allow the development of nonconventional materials, which can be applied not only to the applications suggested in this review but also to diverse fields not yet under consideration. Although the development of these materials has been limited because of the low demand from the industry, it can be expected that as downsizing of devices continues and new concepts of devices emerge, this research area will grow. The problem is only a limited number of ALD processes have been developed for these new materials. One of the main reasons for the lack of systematic research is immature precursor development for these materials. Thus, development of new precursors with various functional groups is a prerequisite for the facile growth of nonconventional materials by ALD. These studies must identify techniques for preventing various drawbacks, including abnormal growth characteristics, impurity incorporation, or damage by deleterious by-products after the ALD reaction. Consequently, intensive studies on the deposition of new materials should be carried out. The research effort would in turn open a new horizon in materials research on nonconventional material synthesis using ALD.

https://doi.org/10.1557/jmr.2019.347 Published online by Cambridge University Press

© Materials Research Society 2019

Acknowledgments

This work was supported by the Materials and Components Technology Development Program of MOTIE/KEIT [10080527, Development of commercialization technology of highly sensitive gas sensor based on chalcogenide 2D nanomaterial], by the Commercialization Promotion Agency for R&D Outcomes (COMPA) funded by the Ministry of Science and ICT (MSIT) [Development of Plasma-based Synthesis Equipment and Process for Two-Dimensional TMDCs], and by the Technology Transfer and Commercialization Program through INNOPOLIS Foundation funded by the Ministry of Science and ICT (2019-GJ-RD-0072/Equipment and Process Development of Large scaled 2D Nanomaterial Synthesis).

References

1. **R.L. Puurunen**: A short history of atomic layer deposition: Tuomo Suntola's atomic layer epitaxy. *Chem. Vap. Deposition* **20**, 332–344 (2014).
2. **H. Kim, H.B.R. Lee, and W.J. Maeng**: Applications of atomic layer deposition to nanofabrication and emerging nanodevices. *Thin Solid Films* **517**, 2563–2580 (2009).
3. **X. Meng, X-Q. Yang, and X. Sun**: Emerging applications of atomic layer deposition for lithium-ion battery studies. *Adv. Mater.* **24**, 3589–3615 (2012).
4. **S.A. Skoog, J.W. Elam, and R.J. Narayan**: Atomic layer deposition: Medical and biological applications. *Int. Mater. Rev.* **58**, 113–129 (2013).
5. **T. Singh, T. Lehnen, T. Leuning, and S. Mathur**: Atomic layer deposition grown MO_x thin films for solar water splitting: Prospects and challenges. *J. Vac. Sci. Technol., A* **33**, 010801 (2015).
6. **S.M. George**: Atomic layer deposition: An overview. *Chem. Rev.* **110**, 111–131 (2010).
7. **J-S. Park, H. Chae, H.K. Chung, and S.I. Lee**: Thin film encapsulation for flexible AM-OLED: A review. *Semicond. Sci. Technol.* **26**, 034001 (2011).
8. **J. Lu, Y. Lei, and J.W. Elam**: Atomic layer deposition of noble metals—New developments in nanostructured catalysts. In *Noble Metals*, ed. Y.-H. Su (InTech, London 2012); pp. 159–178.
9. **H. Kim**: Atomic layer deposition of metal and nitride thin films: Current research efforts and applications for semiconductor device processing. *J. Vac. Sci. Technol., B: Microelectron. Nanometer Struct.* **21**, 2231–2261 (2003).
10. **C. Marichy, M. Bechelany, and N. Pinna**: Atomic layer deposition of nanostructured materials for energy and environmental applications. *Adv. Mater.* **24**, 1017–1032 (2012).
11. **M. Leskelä and M. Ritala**: Atomic layer deposition chemistry: Recent developments and future challenges. *Angew. Chem., Int. Ed.* **42**, 5548–5554 (2003).
12. **T.O. Kääriäinen, M. Kemell, M. Vehkamäki, M.L. Kääriäinen, A. Correia, H.A. Santos, L.M. Bimbo, J. Hirvonen, P. Hoppu, S.M. George, D.C. Cameron, M. Ritala, and M. Leskelä**: Surface modification of acetaminophen particles by atomic layer deposition. *Int. J. Pharm.* **525**, 160–174 (2017).
13. **P. Poodt, D.C. Cameron, E. Dickey, S.M. George, V. Kuznetsov, G.N. Parsons, F. Roozeboom, G. Sundaram, and A. Vermeer**: Spatial atomic layer deposition: A route towards further industrialization of atomic layer deposition. *J. Vac. Sci. Technol., A* **30**, 010802 (2012).
14. **E. Alvaro and A. Yanguas-Gil**: Characterizing the field of atomic layer deposition: Authors, topics, and collaborations. *PLoS One* **13**, 1–19 (2018).
15. **W.J. Maeng, S-J. Park, and H. Kim**: Atomic layer deposition of Ta-based thin films: Reactions of alkylamide precursor with various reactants. *J. Vac. Sci. Technol., B: Microelectron. Nanometer Struct.* **24**, 2276 (2006).
16. **P.D. Ye, G.D. Wilk, J. Kwo, B. Yang, H.J.L. Gossmann, M. Frei, S.N.G. Chu, J.P. Mannaerts, M. Sergent, M. Hong, K.K. Ng, and J. Bude**: GaAs MOSFET with oxide gate dielectric grown by atomic layer deposition. *IEEE Electron Device Lett.* **24**, 209–211 (2003).
17. **E.P. Gusev, C. Cabral, M. Copel, C. D'Emic, and M. Gribelyuk**: Ultrathin HfO_2 films grown on silicon by atomic layer deposition for advanced gate dielectrics applications. *Microelectron. Eng.* **69**, 145–151 (2003).
18. **T. Nam, C.W. Lee, T. Cheon, W.J. Lee, S-H. Kim, S-H. Kwon, H-B-R. Lee, and H. Kim**: Cobalt titanium nitride amorphous metal alloys by atomic layer deposition. *J. Alloys Compd.* **737**, 684–692 (2018).
19. **T.E. Hong, J.H. Jung, S. Yeo, T. Cheon, S.I. Bae, S.H. Kim, S.J. Yeo, H.S. Kim, T.M. Chung, B.K. Park, C.G. Kim, and D.J. Lee**: Highly conformal amorphous W–Si–N thin films by plasma-enhanced atomic layer deposition as a diffusion barrier for Cu metallization. *J. Phys. Chem. C* **119**, 1548–1556 (2015).
20. **H. Kim, C. Detavenier, O. Van Der Straten, S.M. Rossnagel, A.J. Kellock, and D.G. Park**: Robust TaN_x diffusion barrier for Cu-interconnect technology with subnanometer thickness by metal-organic plasma-enhanced atomic layer deposition. *J. Appl. Phys.* **98**, 1–8 (2005).
21. **D-J. Lee, H-M. Kim, J-Y. Kwon, H. Choi, S-H. Kim, and K-B. Kim**: Structural and electrical properties of atomic layer deposited Al-doped ZnO films. *Adv. Funct. Mater.* **21**, 448–455 (2010).
22. **T. Nam, C.W. Lee, H.J. Kim, and H. Kim**: Growth characteristics and properties of Ga-doped ZnO (GZO) thin films grown by thermal and plasma-enhanced atomic layer deposition. *Appl. Surf. Sci.* **295**, 260–265 (2014).
23. **N.P. Dasgupta, S. Neubert, W. Lee, O. Trejo, J.R. Lee, and F.B. Prinz**: Atomic layer deposition of Al-doped ZnO films: Effect of grain orientation on conductivity. *Chem. Mater.* **22**, 4769–4775 (2010).

https://doi.org/10.1557/jmr.2019.347 Published online by Cambridge University Press

© Materials Research Society 2019

24. **D. Kim, T. Nam, J. Park, J. Gatineau, and H. Kim**: Growth characteristics and properties of indium oxide and indium-doped zinc oxide by atomic layer deposition. *Thin Solid Films* **587**, 83–87 (2015).
25. **J. Lu, B. Liu, J.P. Greeley, Z. Feng, J.A. Libera, Y. Lei, M.J. Bedzyk, P.C. Stair, and J.W. Elam**: Porous alumina protective coatings on palladium nanoparticles by self-poisoned atomic layer deposition. *Chem. Mater.* **24**, 2047–2055 (2012).
26. **J. Lee, J. Yoon, H.G. Kim, S. Kang, W-S. Oh, H. Algadi, S. Al-Sayari, B. Shong, S-H. Kim, H. Kim, T. Lee, and H-B-R. Lee**: Highly conductive and flexible fiber for textile electronics obtained by extremely low-temperature atomic layer deposition of Pt. *NPG Asia Mater.* **8**, e331 (2016).
27. **Y.S. Jung, A.S. Cavanagh, L. Gedvilas, N.E. Widjonarko, I.D. Scott, S-H. Lee, G-H. Kim, S.M. George, and A.C. Dillon**: Improved functionality of lithium-ion batteries enabled by atomic layer deposition on the porous microstructure of polymer separators and coating electrodes. *Adv. Energy Mater.* **2**, 1022–1027 (2012).
28. **Z. Li, R.G. Gordon, D.B. Farmer, Y. Lin, and J. Vlassak**: Nucleation and adhesion of ALD copper on cobalt adhesion layers and tungsten nitride diffusion barriers. *Electrochem. Solid-State Lett.* **8**, G182 (2005).
29. **S.T. Christensen, H. Feng, J.L. Libera, N. Guo, J.T. Miller, P.C. Stair, and J.W. Elam**: Supported Ru–Pt bimetallic nanoparticle catalysts prepared by atomic layer deposition. *Nano Lett.* **10**, 3047–3051 (2010).
30. S.I. Association: 2015 ITRS Section 5: More Moore (2015); pp. 1–52.
31. **H. Yaegashi, K. Oyama, A. Hara, S. Natori, and S. Yamauchi**: Overview: Continuous evolution on double-patterning process. *SPIE Adv. Lithogr.* **8325**, 83250B (2012).
32. **K. Kim, U-I. Chung, Y. Park, J. Lee, J. Yeo, and D. Kim**: Extending the DRAM and FLASH memory technologies to 10 nm and beyond. *Opt. Microlithogr. XXV* **8326**, 832605 (2012).
33. **S. Yamahata, N. Shigekawa, K. Kurishima, and Y. Matsuoka**: High-speed carbon-doped-base InP/InGaAs hetero junction bipolar transistors grown by MOCVD. *Electron. Lett.* **31**, 2128–2130 (1995).
34. **T. Choi, H. Jung, C.W. Lee, K.Y. Mun, S.H. Kim, J. Park, and H. Kim**: Growth characteristics of graphene synthesized via chemical vapor deposition using carbon tetrabromide precursor. *Appl. Surf. Sci.* **343**, 128–132 (2015).
35. **R. Ge, X. Wu, M. Kim, J. Shi, S. Sonde, L. Tao, Y. Zhang, J.C. Lee, and D. Akinwande**: Atomristor: Nonvolatile resistance switching in atomic sheets of transition metal dichalcogenides. *Nano Lett.* **18**, 434–441 (2018).
36. **V.K. Sangwan, H.S. Lee, H. Bergeron, I. Balla, M.E. Beck, K.S. Chen, and M.C. Hersam**: Multi-terminal memtransistors from polycrystalline monolayer molybdenum disulfide. *Nature* **554**, 500–504 (2018).
37. **H.E. Lee, J.H. Park, T.J. Kim, D. Im, J.H. Shin, D.H. Kim, B. Mohammad, I.S. Kang, and K.J. Lee**: Novel electronics for flexible and neuromorphic computing. *Adv. Funct. Mater.* **28**, 1–18 (2018).
38. **A. Hirsch**: The era of carbon allotropes. *Nat. Mater.* **9**, 868–871 (2010).
39. **W.I. Milne and J. Robertson**: Carbon, amorphous. In *Encyclopedia of Materials: Science and Technology*, eds. K.H. J. Buschow, R. W. Cahn, M. C. Flemings, B. Ilschner, E. J. Kramer, S. Mahajan, and P. Veyssière (Elsevier, Netherlands, 2001); pp. 900–902.
40. **J. Robertson**: Diamond-like amorphous carbon. *Mater. Sci. Eng., R* **37**, 129–281 (2002).
41. **A. Geim and K. Novoselov**: The rise of graphene. *Nat. Mater.* **6**, 183–191 (2007).
42. **W. Tillmann**: Trends and market perspectives for diamond tools in the construction industry. *Int. J. Refract. Met. Hard Mater.* **18**, 301–306 (2000).
43. **B. Mcenaney**: *Carbon materials for advanced technologies*, Vol. **3** (Elsevier, Netherlands 1999).
44. **I. Electron and D. Society**: Amorphous carbon films as planarization layers deposited by plasma-enhanced chemical vapor deposition. *IEEE Electron Device Lett.* **11**, 391–393 (1990).
45. **W. Liu, D. Mui, T. Lill, M.D. Wang, C. Bencher, M. Kwan, W. Yeh, T. Ebihara, and T. Oga**: Generating sub-30-nm polysilicon gates using PECVD amorphous carbon as hardmask and anti-reflective coating. *Opt. Microlithogr. XVI* **5040**, 841 (2003).
46. **S.J. Park, K. Lee, S.H. Cho, S.H. Choi, S.I. Lee, J.O. Yoo, C.H. Shin, G.J. Min, C.J. Kang, H.K. Cho, and J.T. Moon**: Hard carbon mask for next generation lithographic imaging. In *28th International Symposium on Dry Process* (Nagoya University, Japan, 2006).
47. **C. Wagner and N. Harned**: EUV lithography: Lithography gets extreme. *Nat. Photonics* **4**, 24–26 (2010).
48. **G. Tallents, E. Wagenaars, and G. Pert**: Optical lithography: Lithography at EUV wavelengths. *Nat. Photonics* **4**, 809–811 (2010).
49. **T.D. Horn, R.D. Annual, M. Le, C.E. Ngine, E.R. Conf, and E.R.E. Nce**: Amorphous carbon hard mask for multiple patterning lithography. *J. Microelectron. Eng., Conf.* **21**, 4–6 (2015).
50. **C.Y. Ho, X.J. Lin, H.R. Chien, and C. Lien**: High aspect ratio contact hole etching using relatively transparent amorphous carbon hard mask deposited from propylene. *Thin Solid Films* **518**, 6076–6079 (2010).
51. **K.A. Pears**: A new etching chemistry for carbon hard mask structures. *Microelectron. Eng.* **77**, 255–262 (2005).
52. **M. Kakuchi, M. Hikita, and T. Tamamura**: Amorphous carbon films as resist masks with high reactive ion etching resistance for nanometer lithography. *Appl. Phys. Lett.* **48**, 835–837 (1986).
53. **Y. Chen, Q. Cheng, and W. Kang**: Technological merits, process complexity, and cost analysis of self-aligned multiple patterning. *Opt. Microlithogr. XXV.* **8326**, 832620 (2012).
54. **B. Bhushan**: Chemical, mechanical and tribological characterization of ultra-thin and hard amorphous carbon

https://doi.org/10.1557/jmr.2019.347 Published online by Cambridge University Press

© Materials Research Society 2019

coatings as thin as 3.5 nm: Recent developments. *Diam. Relat. Mater.* **8**, 1985–2015 (1999).

55. **S.M. Rossnagel, A. Sherman, and F. Turner**: Plasma-enhanced atomic layer deposition of Ta and Ti for interconnect diffusion barriers. *J. Vac. Sci. Technol., B: Microelectron. Nanometer Struct.* **18**, 2016 (2000).
56. **H. Kim and S.M. Rossnagel**: Growth kinetics and initial stage growth during plasma-enhanced Ti atomic layer deposition. *J. Vac. Sci. Technol., A* **20**, 802 (2002).
57. **H.C.M. Knoops, S.E. Potts, A.A. Bol, W.M.M. Kessels:** 27 - Atomic Layer Deposition. In *Handbook of Crystal Growth*, ed. T. F. Kuech (Elsevier, Netherlands, 1993); p. 1101–1134.
58. **C.F. Matta, N. Castillo, and R.J. Boyd**: Atomic contributions to bond dissociation energies in aliphatic hydrocarbons. *J. Chem. Phys.* **125**, 204103 (2006).
59. **J.V. Michael, K.P. Lim, S.S. Kumaran, and J.H. Kiefer**: Thermal decomposition of carbon tetrachloride. *J. Phys. Chem.* **97**, 1914–1919 (1993).
60. **Y.J. Kime, D.C. Driscoll, and P.A. Dowben**: The stability of the carbon tetrahalide ions. *J. Chem. Soc., Faraday Trans. 2* **83**, 403–410 (1987).
61. **S.J. Paddison and E. Tschuikow-Roux**: Structures, vibrational frequencies, thermodynamic properties, and bond dissociation energies of the bromomethanes and bromomethyl radicals: An ab initio study. *J. Phys. Chem. A* **102**, 6191–6199 (1998).
62. **B.E. Park, I.K. Oh, C.W. Lee, G. Lee, Y.H. Shin, C. Lansalot-Matras, W. Noh, H. Kim, and H.B.R. Lee**: Effects of Cl-based ligand structures on atomic layer deposited HfO_2. *J. Phys. Chem. C* **120**, 5958–5967 (2016).
63. **T.I. Hukka, R.E. Rawles, and M.P. D'Evelyn**: Novel method for chemical vapor deposition and atomic layer epitaxy using radical chemistry. *Thin Solid Films* **225**, 212–218 (1993).
64. **S.F. Komarov, J.J. Lee, J.B. Hudson, and M.P. D'Evelyn**: Self-limiting diamond growth from alternating CF_x and H fluxes. *Diam. Relat. Mater.* **7**, 1087–1094 (1998).
65. **T. Choi, S. Yeo, J.G. Song, S. Seo, B. Jang, S.H. Kim, and H. Kim**: Hydrogen plasma-enhanced atomic layer deposition of hydrogenated amorphous carbon thin films. *Surf. Coat. Technol.* **344**, 12–20 (2018).
66. **K. Tateno, Y. Kohama, and C. Amano**: Carbon doping and etching effects of CBr_4 during metalorganic chemical vapor deposition of GaAs and AlAs. *J. Cryst. Growth* **172**, 5–12 (1997).
67. **T.J. De Lyon, N.I. Buchan, P.D. Kirchner, J.M. Woodall, G.J. Scilla, and F. Cardone**: High carbon doping efficiency of bromomethanes in gas source molecular beam epitaxial growth of GaAs. *Appl. Phys. Lett.* **58**, 517–519 (1991).
68. **X.J. Zhou, Q. Li, Z.H. He, X. Yang, and K.T. Leung**: Dissociative adsorption and thermal desorption of dibromoethylene on Si(100)2 × 1: Surface mediated dehalogenation and recombinative evolution of HBr. *Surf. Sci.* **543**, L668–L674 (2003).
69. **S.K. Kim, K.M. Kim, D.S. Jeong, W. Jeon, K.J. Yoon, and C.S. Hwang**: Titanium dioxide thin films for next-generation memory devices. *J. Mater. Res.* **28**, 313–325 (2013).
70. **R.P. Bell and S.H. Bauer**: The proton in chemistry. *J. Electrochem. Soc.* **109**, 117C–118C (1962).
71. **H-B-R. Lee and S.F. Bent**: Microstructure-dependent nucleation in atomic layer deposition of Pt on TiO_2. *Chem. Mater.* **24**, 279–286 (2012). Available at: http://pubs.acs.org/doi/abs/10.1021/cm202764b (accessed January 4, 2015).
72. **J.J. Pyeon, C.J. Cho, S.H. Baek, C.Y. Kang, J.S. Kim, D.S. Jeong, and S.K. Kim**: Control of the initial growth in atomic layer deposition of Pt films by surface pretreatment. *Nanotechnology* **26**, 304003 (2015).
73. **M. Popovici, B. Groven, K. Marcoen, Q.M. Phung, S. Dutta, J. Swerts, J. Meersschaut, J.A. Van Den Berg, A. Franquet, A. Moussa, K. Vanstreels, P. Lagrain, H. Bender, M. Jurczak, S. Van Elshocht, A. Delabie, and C. Adelmann**: Atomic layer deposition of ruthenium thin films from (ethylbenzyl) (1-ethyl-1,4-cyclohexadienyl) Ru: Process characteristics, surface chemistry, and film properties. *Chem. Mater.* **29**, 4654–4666 (2017).
74. **L. Baker, A.S. Cavanagh, D. Seghete, S.M. George, A.J.M. MacKus, W.M.M. Kessels, Z.Y. Liu, and F.T. Wagner**: Nucleation and growth of Pt atomic layer deposition on Al_2O_3 substrates using (methylcyclopentadienyl)-trimethyl platinum and O_2 plasma. *J. Appl. Phys.* **109**, 084333 (2011).
75. **J. Dendooven, R.K. Ramachandran, K. Devloo-Casier, G. Rampelberg, M. Filez, H. Poelman, G.B. Marin, E. Fonda, and C. Detavernier**: Low-temperature atomic layer deposition of platinum using (methylcyclopentadienyl)trimethylplatinum and ozone. *J. Phys. Chem. C* **117**, 20557–20561 (2013).
76. **H-B-R. Lee, S.H. Baeck, T.F. Jaramillo, and S.F. Bent**: Growth of Pt nanowires by atomic layer deposition on highly ordered pyrolytic graphite. *Nano Lett.* **13**, 457–463 (2013).
77. **H-B-R. Lee, M.N. Mullings, X. Jiang, B.M. Clemens, and S.F. Bent**: Nucleation-controlled growth of nanoparticles by atomic layer deposition. *Chem. Mater.* **24**, 4051–4059 (2012).
78. **L. Baker, A.S. Cavanagh, J. Yin, S.M. George, A. Kongkanand, and F.T. Wagner**: Growth of continuous and ultrathin platinum films on tungsten adhesion layers using atomic layer deposition techniques. *Appl. Phys. Lett.* **101**, 111601 (2012).
79. **C.T. Campbell**: Ultrathin metal films and particles on oxide surfaces: Structural, electronic and chemisorptive properties. *Surf. Sci. Rep.* **27**, 1–111 (1997).
80. **J. Heo, S.J. Won, D. Eom, S.Y. Lee, Y.B. Ahn, C.S. Hwang, and H.J. Kim**: The role of the methyl and hydroxyl groups of low-*k* dielectric films on the nucleation of ruthenium by ALD. *Electrochem. Solid-State Lett.* **11**, 210–213 (2008).
81. **C. Liu, C.C. Wang, C.C. Kei, Y.C. Hsueh, and T.P. Perng**: Atomic layer deposition of platinum nanoparticles on carbon nanotubes for application in proton-exchange membrane fuel cells. *Small* **5**, 1535–1538 (2009).

https://doi.org/10.1557/jmr.2019.347 Published online by Cambridge University Press

© Materials Research Society 2019

82. **Y.C. Hsueh, C. Te Hu, C.C. Wang, C. Liu, and T.P. Perng**: Deposition of Pt nanoparticles on oxygen plasma treated carbon nanotubes by atomic layer deposition. *ECS Trans.* **16**, 855–862 (2008).
83. **P. K. Chu and L. Li**: Characterization of amorphous and nanocrystalline carbon films. *Mater. Chem. Phys.* **96**, 253–277 (2006).
84. **R.U.R. Sagar, X. Zhang, C. Xiong, and Y. Yu**: Semiconducting amorphous carbon thin films for transparent conducting electrodes. *Carbon* **76**, 64–70 (2014).
85. **R. Dominko, M. Bele, M. Gaberscek, M. Remskar, D. Hanzel, S. Pejovnik, and J. Jamnik**: Impact of the carbon coating thickness on the electrochemical performance of $LiFePO_4$/C composites. *J. Electrochem. Soc.* **152**, 607–610 (2005).
86. **I.D. Scott, Y.S. Jung, A.S. Cavanagh, Y. Yan, A.C. Dillon, S.M. George, and S.H. Lee**: Ultrathin coatings on nano-$LiCoO_2$ for Li-ion vehicular applications. *Nano Lett.* **11**, 414–418 (2011).
87. **X. Zhu, X. Yang, C. Lv, S. Guo, J. Li, Z. Zheng, H. Zhu, and D. Yang**: New approach to create TiO_2(B)/carbon core/shell nanotubes: Ideal structure for enhanced lithium ion storage. *ACS Appl. Mater. Interfaces* **8**, 18815–18821 (2016).
88. **P.S. Goley and M.K. Hudait**: Germanium based field-effect transistors: Challenges and opportunities. *Materials* **7**, 2301–2339 (2014).
89. **S.H. Shin, H. Jiang, W. Ahn, H. Wu, W. Chung, P.D. Ye, and M.A. Alam**: Performance potential of Ge CMOS technology from a material-device-circuit perspective. *IEEE Trans. Electron Devices* **65**, 1679–1684 (2018).
90. **Y. Kamata**: High-*k*/Ge MOSFETs for future nanoelectronics. *Mater. Today* **11**, 30–38 (2008).
91. **D. Bodlaki, H. Yamamoto, D.H. Waldeck, and E. Borguet**: Ambient stability of chemically passivated germanium interfaces. *Surf. Sci.* **543**, 63–74 (2003).
92. **Q. Xie, S. Deng, M. Schaekers, D. Lin, M. Caymax, A. Delabie, X.P. Qu, Y.L. Jiang, D. Deduytsche, and C. Detavernier**: Germanium surface passivation and atomic layer deposition of high-*k* dielectrics—A tutorial review on Ge-based MOS capacitors. *Semicond. Sci. Technol.* **27**, 074012 (2012).
93. **I.K. Oh, K. Kim, Z. Lee, J.G. Song, C.W. Lee, D. Thompson, H.B.R. Lee, W.H. Kim, W.J. Maeng, and H. Kim**: In situ surface cleaning on a Ge substrate using TMA and $MgCp_2$ for HfO_2-based gate oxides. *J. Mater. Chem. C* **3**, 4852–4858 (2015).
94. **M. Kanematsu, S. Shibayama, M. Sakashita, W. Takeuchi, O. Nakatsuka, and S. Zaima**: Effect of GeO_2 deposition temperature in atomic layer deposition on electrical properties of Ge gate stack. *Jpn. J. Appl. Phys.* **55**, 1–6 (2016).
95. **A. Molle, S. Spiga, and M. Fanciulli**: Stability and interface quality of GeO_2 films grown on Ge by atomic oxygen assisted deposition. *J. Chem. Phys.* **129**, 1–5 (2008).
96. **S. Takagi, T. Maeda, N. Taoka, M. Nishizawa, Y. Morita, K. Ikeda, Y. Yamashita, M. Nishikawa, H. Kumagai, R. Nakane, S. Sugahara, and N. Sugiyama**: Gate dielectric formation and MIS interface characterization on Ge. *Microelectron. Eng.* **84**, 2314–2319 (2007).
97. **N. Greenwood and A. Earnshaw**: *Chemistry of the Elements* (Butterworth-Heinemann, 1997).
98. **S. Shibayama, T. Yoshida, K. Kato, M. Sakashita, W. Takeuchi, N. Taoka, O. Nakatsuka, and S. Zaima**: Formation of chemically stable GeO_2 on the Ge surface with pulsed metal-organic chemical vapor deposition. *Appl. Phys. Lett.* **106**, 1–5 (2015).
99. **F. Bellenger, B. De Jaeger, C. Merckling, M. Houssa, J. Penaud, L. Nyns, E. Vrancken, M. Caymax, M. Meuris, T. Hoffmann, K. De Meyer, and M. Heyns**: High FET performance for a future CMOS GeO_2-based technology. *IEEE Electron Device Lett.* **31**, 402–404 (2010).
100. **Y. Seo, T.I. Lee, C.M. Yoon, B.E. Park, W.S. Hwang, H. Kim, H.Y. Yu, and B.J. Cho**: The impact of an ultrathin Y_2O_3 layer on GeO_2 passivation in Ge MOS gate stacks. *IEEE Trans. Electron Devices* **64**, 3303–3307 (2017).
101. **T. Busani, H. Plantier, R.A.B. Devine, C. Hernandez, and Y. Campidelli**: Growth and characterization of GeO_2 films obtained by plasma anodization of epitaxial Ge films. *J. Appl. Phys.* **85**, 4262–4264 (1999).
102. **K. Kita, C.H. Lee, T. Nishimura, K. Nagashio, and A. Toriumi**: Control of properties of GeO_2 films and Ge/GeO_2 interfaces by the suppression of GeO volatilization. *ECS Trans.* **19**, 101–116 (2009).
103. **H. Weis, M. Beckers, M. Wuttig, T. Lange, and W. Njoroge**: Physical properties of thin GeO_2 films produced by reactive DC magnetron sputtering. *Thin Solid Films* **365**, 82–89 (2000).
104. **N.R. Murphy, J.T. Grant, L. Sun, J.G. Jones, R. Jakubiak, V. Shutthanandan, and C.V. Ramana**: Correlation between optical properties and chemical composition of sputter-deposited germanium oxide (GeO_x) films. *Opt. Mater.* **36**, 1177–1182 (2014).
105. **M. Perego, G. Scarel, M. Fanciulli, I.L. Fedushkin, and A.A. Skatova**: Fabrication of GeO_2 layers using a divalent Ge precursor. *Appl. Phys. Lett.* **90**, 1–4 (2007).
106. **J.S. Jung, D.H. Kim, J.H. Shin, and J.G. Kang**: Atomic layer deposition of GeO_2 thin films on Si(100) using Ge(*N*,*N*′-R,R-en)$(NMe_2)_2$ (where R = isopropyl and *t*-butyl) precursors. *Bull. Korean Chem. Soc.* **36**, 1953–1954 (2015).
107. **S. Kar**: *High Permittivity Gate Dielectric Materials*, 1st ed. (Springer-Verlag, Berlin, Heidelberg, 2013).
108. **A. Ohta, H. Nakagawa, H. Murakami, S. Higashi, and S. Miyazaki**: Photoemission study of ultrathin GeO_2/Ge heterostructures formed by UV-O_3 oxidation. *e-J. Surf. Sci. Nanotechnol.* **4**, 174–179 (2006).
109. **C.L. Dezelah IV, O.M. El-Kadri, K. Kukli, K. Arstila, R.J. Baird, J. Lu, L. Niinistö, and C.H. Winter**: A low valent metalorganic precursor for the growth of tungsten nitride thin films by atomic layer deposition. *J. Mater. Chem.* **17**, 1109–1116 (2007).

https://doi.org/10.1557/jmr.2019.347 Published online by Cambridge University Press

© Materials Research Society 2019

110. **C.L. Dezelah IV, O.M. El-Kadri, I.M. Szilágyi, J.M. Campbell, K. Arstila, L. Niinistö, and C.H. Winter**: Atomic layer deposition of tungsten(III) oxide thin films from $W_2(NMe_2)_6$ and water: Precursor-based control of oxidation state in the thin film material. *J. Am. Chem. Soc.* **128**, 9638–9639 (2006).
111. **C.M. Yoon, I.K. Oh, Y. Lee, J.G. Song, S.J. Lee, J.M. Myoung, H.G. Kim, H.S. Moon, B. Shong, H.B.R. Lee, and H. Kim**: Water-erasable memory device for security applications prepared by the atomic layer deposition of GeO_2. *Chem. Mater.* **30**, 830–840 (2018).
112. **J.S. Kachian, K.T. Wong, and S.F. Bent**: Periodic trends in organic functionalization of group IV semiconductor surfaces. *Acc. Chem. Res.* **43**, 346–355 (2010).
113. **Y. Oniki, H. Koumo, Y. Iwazaki, and T. Ueno**: Evaluation of GeO desorption behavior in the metal/GeO_2/Ge structure and its improvement of the electrical characteristics. *J. Appl. Phys.* **107**, 124113 (2010).
114. **S.N.A. Murad, P.T. Baine, D.W. McNeill, S.J.N. Mitchell, B.M. Armstrong, M. Modreanu, G. Hughes, and R.K. Chellappan**: Optimisation and scaling of interfacial GeO_2 layers for high-*k* gate stacks on germanium and extraction of dielectric constant of GeO_2. *Solid State Electron.* **78**, 136–140 (2012).
115. **A.A.F. Novoselov, A.K. Geim, S.V. Morozov, D. Jiang, Y. Zhang, S.V. Dubonos, and I.V. Grigorieva**: Electric field effect in atomically thin carbon films. *Science* **666**, 666–669 (2013).
116. **K.I. Bolotin**: Electronic transport in graphene: Towards high mobility. In *Graphene*, eds. V. Skákalová and A. B. Kaiser (Woodhead Publishing, Cambridge, 2014); pp. 199–227.
117. **S. Manzeli, D. Ovchinnikov, D. Pasquier, O.V. Yazyev, and A. Kis**: 2D transition metal dichalcogenides. *Nat. Rev. Mater.* **2**, 17033 (2017).
118. **M. Chhowalla, H.S. Shin, G. Eda, L-J. Li, K.P. Loh, and H. Zhang**: The chemistry of two-dimensional layered transition metal dichalcogenide nanosheets. *Nat. Chem.* **5**, 263–275 (2013).
119. **P.C. Yeh, W. Jin, N. Zaki, D. Zhang, J.T. Liou, J.T. Sadowski, A. Al-Mahboob, J.I. Dadap, I.P. Herman, P. Sutter, and R.M. Osgood**: Layer-dependent electronic structure of an atomically heavy two-dimensional dichalcogenide. *Phys. Rev. B: Condens. Matter Mater. Phys.* **91**, 1–6 (2015).
120. **H. Li, J. Wu, Z. Yin, and H. Zhang**: Preparation and applications of mechanically exfoliated single-layer and multilayer MoS_2 and WSe_2 nanosheets. *Acc. Chem. Res.* **47**, 1067–1075 (2014).
121. **K.F. Mak, C. Lee, J. Hone, J. Shan, and T.F. Heinz**: Atomically thin MoS_2: A new direct-gap semiconductor. *Phys. Rev. Lett.* **105**, 2–5 (2010).
122. **C. Tan and H. Zhang**: Two-dimensional transition metal dichalcogenide nanosheet-based composites. *Chem. Soc. Rev.* **44**, 2713–2731 (2015).
123. **B. Radisavljevic, A. Radenovic, J. Brivio, V. Giacometti, and A. Kis**: Single-layer MoS_2 transistors. *Nat. Nanotechnol.* **6**, 147–150 (2011).
124. **K.F. Mak and J. Shan**: Photonics and optoelectronics of 2D semiconductor transition metal dichalcogenides. *Nat. Photonics* **10**, 216–226 (2016).
125. **V.W. Brar, M.C. Sherrott, and D. Jariwala**: Emerging photonic architectures in two-dimensional opto-electronics. *Chem. Soc. Rev.* **47**, 6824–6844 (2018).
126. **K. Kaasbjerg, K.S. Thygesen, and K.W. Jacobsen**: Phonon-limited mobility in n-type single-layer MoS_2 from first principles. *Phys. Rev. B: Condens. Matter Mater. Phys.* **85**, 1–16 (2012).
127. **M.N. Ali, J. Xiong, S. Flynn, J. Tao, Q.D. Gibson, L.M. Schoop, T. Liang, N. Haldolaarachchige, M. Hirschberger, N.P. Ong, and R.J. Cava**: Large, non-saturating magnetoresistance in WTe_2. *Nature* **514**, 205–208 (2014).
128. **C. Rice, R.J. Young, R. Zan, U. Bangert, D. Wolverson, T. Georgiou, R. Jalil, and K.S. Novoselov**: Raman-scattering measurements and first-principles calculations of strain-induced phonon shifts in monolayer MoS_2. *Phys. Rev. B: Condens. Matter Mater. Phys.* **87**, 1–5 (2013).
129. **X. Xu, W. Yao, D. Xiao, and T.F. Heinz**: Spin and pseudospins in layered transition metal dichalcogenides. *Nat. Phys.* **10**, 343–350 (2014).
130. **G. Eda, H. Yamaguchi, D. Voiry, T. Fujita, M. Chen, and M. Chhowalla**: Photoluminescence from chemically exfoliated MoS_2. *Nano Lett.* **11**, 5111–5116 (2011).
131. **A.V. Kolobov and J. Tominaga**: *Two-Dimensional Transition-Metal Dichalcogenides* (Springer, 2016).
132. **J. Sun, X. Li, W. Guo, M. Zhao, X. Fan, Y. Dong, C. Xu, J. Deng, and Y. Fu**: Synthesis methods of two-dimensional MoS_2: A brief review. *Crystals* **7**, 18–37 (2017).
133. **S. Najmaei, Z. Liu, W. Zhou, X. Zou, G. Shi, S. Lei, B.I. Yakobson, J.C. Idrobo, P.M. Ajayan, and J. Lou**: Vapour phase growth and grain boundary structure of molybdenum disulphide atomic layers. *Nat. Mater.* **12**, 754–759 (2013).
134. **J.G. Song, J. Park, W. Lee, T. Choi, H. Jung, C.W. Lee, S.H. Hwang, J.M. Myoung, J.H. Jung, S.H. Kim, C. Lansalot-Matras, and H. Kim**: Layer-controlled, wafer-scale, and conformal synthesis of tungsten disulfide nanosheets using atomic layer deposition. *ACS Nano* **7**, 11333–11340 (2013).
135. **D. Ovchinnikov, A. Allain, Y.S. Huang, D. Dumcenco, and A. Kis**: Electrical transport properties of single-layer WS_2. *ACS Nano* **8**, 8174–8181 (2014).
136. **A. Chernikov, A.M. Van Der Zande, H.M. Hill, A.F. Rigosi, A. Velauthapillai, J. Hone, and T.F. Heinz**: Electrical tuning of exciton binding energies in monolayer WS_2. *Phys. Rev. Lett.* **115**, 1–6 (2015).
137. **H.C. Kim, H. Kim, J.U. Lee, H.B. Lee, D.H. Choi, J.H. Lee, W.H. Lee, S.H. Jhang, B.H. Park, H. Cheong, S.W. Lee, and H.J. Chung**: Engineering optical and electronic properties of WS_2 by varying the number of layers. *ACS Nano* **9**, 6854–6860 (2015).
138. **C. Cong, J. Shang, Y. Wang, and T. Yu**: Optical properties of 2D semiconductor WS_2. *Adv. Opt. Mater.* **6**, 1–15 (2018).

https://doi.org/10.1557/jmr.2019.347 Published online by Cambridge University Press

© Materials Research Society 2019

139. **Y. Kajino, K. Oto, and Y. Yamada**: Modification of optical properties in monolayer WS_2 on dielectric substrates by coulomb engineering. *J. Phys. Chem. C* **123**, 14097–14102 (2019).
140. **G. Plechinger, P. Nagler, A. Arora, A. Granados Del Águila, M.V. Ballottin, T. Frank, P. Steinleitner, M. Gmitra, J. Fabian, P.C.M. Christianen, R. Bratschitsch, C. Schüller, and T. Korn**: Excitonic valley effects in monolayer WS_2 under high magnetic fields. *Nano Lett.* **16**, 7899–7904 (2016).
141. **Y. Ma, Y. Dai, M. Guo, C. Niu, J. Lu, and B. Huang**: Electronic and magnetic properties of perfect, vacancy-doped, and nonmetal adsorbed $MoSe_2$, $MoTe_2$, and WS_2 monolayers. *Phys. Chem. Chem. Phys.* **13**, 15546–15553 (2011).
142. **J. Duan, S. Chen, B.A. Chambers, G.G. Andersson, and S.Z. Qiao**: 3D WS_2 nanolayers@heteroatom-doped graphene films as hydrogen evolution catalyst electrodes. *Adv. Mater.* **27**, 4234–4241 (2015).
143. **M.A. Lukowski, A.S. Daniel, C.R. English, F. Meng, A. Forticaux, R.J. Hamers, and S. Jin**: Highly active hydrogen evolution catalysis from metallic WS_2 nanosheets. *Energy Environ. Sci.* **7**, 2608–2613 (2014).
144. **H.R. Gutiérrez, N. Perea-López, A.L. Elías, A. Berkdemir, B. Wang, R. Lv, F. López-Urías, V.H. Crespi, H. Terrones, and M. Terrones**: Extraordinary room-temperature photoluminescence in triangular WS_2 monolayers. *Nano Lett.* **13**, 3447–3454 (2013).
145. **A. Berkdemir, H.R. Gutiérrez, A.R. Botello-Méndez, N. Perea-López, A.L. Elías, C.I. Chia, B. Wang, V.H. Crespi, F. López-Urías, J.C. Charlier, H. Terrones, and M. Terrones**: Identification of individual and few layers of WS_2 using Raman spectroscopy. *Sci. Rep.* **3**, 1–8 (2013).
146. **A. Molina-Sánchez and L. Wirtz**: Phonons in single-layer and few-layer MoS_2 and WS_2. *Phys. Rev. B: Condens. Matter Mater. Phys.* **84**, 1–8 (2011).
147. **Y.H. Lee, L. Yu, H. Wang, W. Fang, X. Ling, Y. Shi, C. Te Lin, J.K. Huang, M.T. Chang, C.S. Chang, M. Dresselhaus, T. Palacios, L.J. Li, and J. Kong**: Synthesis and transfer of single-layer transition metal disulfides on diverse surfaces. *Nano Lett.* **13**, 1852–1857 (2013).
148. **Y. Zhan, Z. Liu, S. Najmaei, P.M. Ajayan, and J. Lou**: Large-area vapor-phase growth and characterization of MoS_2 atomic layers on a SiO_2 substrate. *Small* **8**, 966–971 (2012).
149. **F. Chen, J. Xia, D.K. Ferry, and N. Tao**: Dielectric screening enhanced performance in graphene FET. *Nano Lett.* **9**, 2571–2574 (2009).
150. **D. Jena and A. Konar**: Enhancement of carrier mobility in semiconductor nanostructures by dielectric engineering. *Phys. Rev. Lett.* **98**, 1–4 (2007).
151. **D. Lembke and A. Kis**: Breakdown of high-performance monolayer MoS_2 transistors. *ACS Nano* **6**, 10070–10075 (2012).
152. **Y. Zongyou, L. Hai, L. Hong, J. Lin, S. Yumeng, S. Yinghui, L. Gang, Z. Qing, C. Xiaodong, and Z. Hua**: Single-layer MoS_2 phototransistors. *ACS Nano* **6**, 74–80 (2012). Available at: http://pubs.acs.org/doi/abs/10.1021/nn2024557 (accessed May 20, 2014).
153. **J.G. Song, G.H. Ryu, S.J. Lee, S. Sim, C.W. Lee, T. Choi, H. Jung, Y. Kim, Z. Lee, J.M. Myoung, C. Dussarrat, C. Lansalot-Matras, J. Park, H. Choi, and H. Kim**: Controllable synthesis of molybdenum tungsten disulfide alloy for vertically composition-controlled multilayer. *Nat. Commun.* **6**, 1–10 (2015).
154. **P.E. Blackburn, M. Hoch, and H.L. Johnston**: The vaporization of molybdenum and tungsten oxides. *J. Phys. Chem.* **62**, 769–773 (1958).
155. **B.D. Keller, A. Bertuch, J. Provine, G. Sundaram, N. Ferralis, and J.C. Grossman**: Process control of atomic layer deposition molybdenum oxide nucleation and sulfidation to large-area MoS_2 monolayers. *Chem. Mater.* **29**, 2024–2032 (2017).
156. **M. Bernardi, M. Palummo, and J.C. Grossman**: Extraordinary sunlight absorption and one nanometer thick photovoltaics using two-dimensional monolayer materials. *Nano Lett.* **13**, 3664–3670 (2013).
157. **Q.H. Wang, K. Kalantar-Zadeh, A. Kis, J.N. Coleman, and M.S. Strano**: Electronics and optoelectronics of two-dimensional transition metal dichalcogenides. *Nat. Nanotechnol.* **7**, 699–712 (2012).
158. **A. Kutana, E.S. Penev, and B.I. Yakobson**: Engineering electronic properties of layered transition-metal dichalcogenide compounds through alloying. *Nanoscale* **6**, 5820–5825 (2014).
159. **S. Susarla, A. Kutana, J.A. Hachtel, V. Kochat, A. Apte, R. Vajtai, J.C. Idrobo, B.I. Yakobson, C.S. Tiwary, and P.M. Ajayan**: Quaternary 2D transition metal dichalcogenides (TMDs) with tunable bandgap. *Adv. Mater.* **29**, 1–8 (2017).
160. **J.R. Bakke, J.T. Tanskanen, H.J. Jung, R. Sinclair, and S.F. Bent**: Atomic layer deposition of $Cd_xZn_{1-x}S$ films. *J. Mater. Chem.* **21**, 743–751 (2011).
161. **P. Banerjee, W.J. Lee, K.R. Bae, S.B. Lee, and G.W. Rubloff**: Structural, electrical, and optical properties of atomic layer deposition Al-doped ZnO films. *J. Appl. Phys.* **108**, 043504 (2010).
162. **C. Adelmann, H. Tielens, D. Dewulf, A. Hardy, D. Pierreux, J. Swerts, E. Rosseel, X. Shi, M.K. Van Bael, J.A. Kittl, and S. Van Elshocht**: Atomic layer deposition of Gd-doped HfO_2 thin films. *J. Electrochem. Soc.* **157**, 105–110 (2010).
163. **E. Thimsen, S.C. Riha, S.V. Baryshev, A.B.F. Martinson, J.W. Elam, and M.J. Pellin**: Atomic layer deposition of the quaternary chalcogenide Cu_2 $ZnSnS_4$. *Chem. Mater.* **24**, 3188–3196 (2012).
164. **E. Ahvenniemi, M. Matvejeff, and M. Karppinen**: Atomic layer deposition of quaternary oxide (La, Sr)$CoO_{3-\delta}$ thin films. *Dalton Trans.* **44**, 8001–8006 (2015).
165. **W.J. Yin, X.G. Gong, and S.H. Wei**: Origin of the unusually large band-gap bowing and the breakdown of the band-edge distribution rule in the Sn_xGe_{1-x} alloys. *Phys. Rev. B: Condens. Matter Mater. Phys.* **78**, 1–4 (2008).
166. **Y. Chen, J. Xi, D.O. Dumcenco, Z. Liu, K. Suenaga, D. Wang, Z. Shuai, Y.S. Huang, and L. Xie**: Tunable band gap photoluminescence from atomically thin transition-metal dichalcogenide alloys. *ACS Nano* **7**, 4610–4616 (2013).

https://doi.org/10.1557/jmr.2019.347 Published online by Cambridge University Press

© Materials Research Society 2019

167. **X. Hong, J. Kim, S.F. Shi, Y. Zhang, C. Jin, Y. Sun, S. Tongay, J. Wu, Y. Zhang, and F. Wang**: Ultrafast charge transfer in atomically thin MoS_2/WS_2 heterostructures. *Nat. Nanotechnol.* **9**, 682–686 (2014).
168. **K. Koåmider and J. Fernández-Rossier**: Electronic properties of the MoS_2–WS_2 heterojunction. *Phys. Rev. B: Condens. Matter Mater. Phys.* **87**, 2–5 (2013).
169. **S. Tongay, W. Fan, J. Kang, J. Park, U. Koldemir, J. Suh, D.S. Narang, K. Liu, J. Ji, J. Li, R. Sinclair, and J. Wu**: Tuning interlayer coupling in large-area heterostructures with CVD-grown MoS_2 and WS_2 monolayers. *Nano Lett.* **14**, 3185–3190 (2014).
170. **Y. Yu, S. Hu, L. Su, L. Huang, Y. Liu, Z. Jin, A.A. Purezky, D.B. Geohegan, K.W. Kim, Y. Zhang, and L. Cao**: Equally efficient interlayer exciton relaxation and improved absorption in epitaxial and nonepitaxial MoS_2/WS_2 heterostructures. *Nano Lett.* **15**, 486–491 (2015).
171. **Y. Gong, J. Lin, X. Wang, G. Shi, S. Lei, Z. Lin, X. Zou, G. Ye, R. Vajtai, B.I. Yakobson, H. Terrones, M. Terrones, B.K. Tay, J. Lou, S.T. Pantelides, Z. Liu, W. Zhou, and P.M. Ajayan**: Vertical and in-plane heterostructures from WS_2/MoS_2 monolayers. *Nat. Mater.* **13**, 1135–1142 (2014).
172. **Z. Lin, Y. Zhao, C. Zhou, R. Zhong, X. Wang, Y.H. Tsang, and Y. Chai**: Controllable growth of large-size crystalline MoS_2 and resist-free transfer assisted with a Cu thin film. *Sci. Rep.* **5**, 1–10 (2015).
173. **L.K. Tan, B. Liu, J.H. Teng, S. Guo, H.Y. Low, and K.P. Loh**: Atomic layer deposition of a MoS_2 film. *Nanoscale* **6**, 10584–10588 (2014).
174. **T. Jurca, M.J. Moody, A. Henning, J.D. Emery, B. Wang, J.M. Tan, T.L. Lohr, L.J. Lauhon, and T.J. Marks**: Low-temperature atomic layer deposition of MoS_2 films. *Angew. Chem., Int. Ed.* **56**, 4991–4995 (2017).
175. **D.K. Nandi, S. Sahoo, S. Sinha, S. Yeo, H. Kim, R.N. Bulakhe, J. Heo, J.J. Shim, and S.H. Kim**: Highly uniform atomic layer-deposited MoS_2@3D-Ni-foam: A novel approach to prepare an electrode for supercapacitors. *ACS Appl. Mater. Interfaces* **9**, 40252–40264 (2017).
176. **M. Mattinen, T. Hatanpää, T. Sarnet, K. Mizohata, K. Meinander, P.J. King, L. Khriachtchev, J. Räisänen, M. Ritala, and M. Leskelä**: Atomic layer deposition of crystalline MoS_2 thin films: New molybdenum precursor for low-temperature film growth. *Adv. Mater. Interfaces* **4**, 1–11 (2017).
177. **J.J. Pyeon, S.H. Kim, D.S. Jeong, S.H. Baek, C.Y. Kang, J.S. Kim, and S.K. Kim**: Wafer-scale growth of MoS_2 thin films by atomic layer deposition. *Nanoscale* **8**, 10792–10798 (2016).
178. **Z. Jin, S. Shin, D.H. Kwon, S.J. Han, and Y.S. Min**: Novel chemical route for atomic layer deposition of MoS_2 thin film on SiO_2/Si substrate. *Nanoscale* **6**, 14453–14458 (2014).
179. **Y. Kim, J.G. Song, Y.J. Park, G.H. Ryu, S.J. Lee, J.S. Kim, P.J. Jeon, C.W. Lee, W.J. Woo, T. Choi, H. Jung, H.B.R. Lee, J.M. Myoung, S. Im, Z. Lee, J.H. Ahn, J. Park, and H. Kim**: Self-limiting layer synthesis of transition metal dichalcogenides. *Sci. Rep.* **6**, 1–8 (2016).
180. **K. Park, Y. Kim, J.G. Song, S.J. Kim, C. Wanlee, G.H. Ryu, Z. Lee, J. Park, and H. Kim**: Uniform, large-area self-limiting layer synthesis of tungsten diselenide. *2D Mater.* **3**, 014004 (2016).
181. **S. McDonnell, B. Brennan, A. Azcatl, N. Lu, H. Dong, C. Buie, J. Kim, C.L. Hinkle, M.J. Kim, and R.M. Wallace**: HfO_2 on MoS_2 by atomic layer deposition: Adsorption mechanisms and thickness scalability. *ACS Nano* **7**, 10354–10361 (2013).
182. **S.J. McDonnell and R.M. Wallace**: UV-ozone functionalization of 2D materials. *Jom* **71**, 224–237 (2019).
183. **A. Castellanos-Gomez, E. Cappelluti, R. Roldán, N. Agraït, F. Guinea, and G. Rubio-Bollinger**: Electric-field screening in atomically thin layers of MoS_2: The role of interlayer coupling. *Adv. Mater.* **25**, 899–903 (2013).
184. **J. Huang, L. Yang, D. Liu, J. Chen, Q. Fu, Y. Xiong, F. Lin, and B. Xiang**: Large-area synthesis of monolayer WSe_2 on a SiO_2/Si substrate and its device applications. *Nanoscale* **7**, 4193–4198 (2015).
185. **R. Dong and I. Kuljanishvili**: Review article: Progress in fabrication of transition metal dichalcogenides heterostructure systems. *J. Vac. Sci. Technol., B: Nanotechnol. Microelectron.: Mater., Process., Meas., Phenom.* **35**, 030803 (2017).
186. **M.M. Furchi, A. Pospischil, F. Libisch, J. Burgdörfer, and T. Mueller**: Photovoltaic effect in an electrically tunable Van der Waals heterojunction. *Nano Lett.* **14**, 4785–4791 (2014).
187. **C.H. Lee, G.H. Lee, A.M. Van Der Zande, W. Chen, Y. Li, M. Han, X. Cui, G. Arefe, C. Nuckolls, T.F. Heinz, J. Guo, J. Hone, and P. Kim**: Atomically thin p–n junctions with van der Waals heterointerfaces. *Nat. Nanotechnol.* **9**, 676–681 (2014).
188. **H. Fang, C. Battaglia, C. Carraro, S. Nemsak, B. Ozdol, J.S. Kang, H.A. Bechtel, S.B. Desai, F. Kronast, A.A. Unal, G. Conti, C. Conlon, G.K. Palsson, M.C. Martin, A.M. Minor, C.S. Fadley, E. Yablonovitch, R. Maboudian, and A. Javey**: Strong interlayer coupling in van der Waals heterostructures built from single-layer chalcogenides. *Proc. Natl. Acad. Sci. U. S. A.* **111**, 6198–6202 (2014).
189. **Y. Kim, D. Choi, W.J. Woo, J.B. Lee, G.H. Ryu, J.H. Lim, S. Lee, Z. Lee, S. Im, J-H. Ahn, W-H. Kim, J. Park, and H. Kim**: Synthesis of two-dimensional MoS_2/graphene heterostructure by atomic layer deposition using MoF_6 precursor. *Appl. Surf. Sci.* **494**, 591–599 (2019).
190. **L. Zhan, W. Wan, Z. Zhu, Y. Xu, T.M. Shih, C. Zhang, W. Lin, X. Li, Z. Zhao, H. Ying, Q. Yao, Y. Zheng, Z. Zhu, and W. Cai**: Centimeter-scale nearly single-crystal monolayer MoS_2 via self-limiting vapor deposition epitaxy. *J. Phys. Chem. C* **121**, 4703–4707 (2017).
191. **K. Kim, H.B.R. Lee, R.W. Johnson, J.T. Tanskanen, N. Liu, M.G. Kim, C. Pang, C. Ahn, S.F. Bent, and Z. Bao**: Selective metal deposition at graphene line defects by atomic layer deposition. *Nat. Commun.* **5**, 1–9 (2014).
192. **K.Y. Ko, S. Lee, K. Park, Y. Kim, W.J. Woo, D. Kim, J.G. Song, J. Park, J.H. Kim, Z. Lee, and H. Kim**: High-performance gas sensor using a large-area $WS_{2x}Se_{2-2x}$ alloy for low-power operation wearable applications. *ACS Appl. Mater. Interfaces* **10**, 34163–34171 (2018).

https://doi.org/10.1557/jmr.2019.347 Published online by Cambridge University Press

© Materials Research Society 2019